SSRG International Journal of Electronics and Communication Engineering
ISSN: 2348-8549/ https://doi.org/10.14445/23488549/IJECE-V13I4P128

Volume 13 Issue 4, 348-370, April 2026

Original Article

An Entropy-Based Adaptive Quantum Image Representation (EBA-QR) for Efficient Multimodal Image Processing

Vrushali Nikam[1], Shirish Sane[2]

[1]*Computer Engineering, Research Scholar, MET's BKCIOE, Nashik, Maharashtra, India.*
[2]*Computer Engineering, Professor and Principal, GES's R H Sapat COE, Nashik, Maharashtra, India.*

[1]*Corresponding Author : vrushali.nikam@ges-coengg.org*

Received: 24 January 2026 Revised: 24 February 2026 Accepted: 25 March 2026 Published: 30 April 2026

Abstract *- Superposition, entanglement, and quantum parallelism can be utilized in Quantum Image Processing (QIP) as a promising paradigm for expediting large-scale visual computing workloads. However, the majority of existing content-agnostic Quantum Image Representation (QIR) models allocate an equal amount of computational resources to individual pixels, irrespective of their semantic significance. This approach poses particular challenges to Noisy Intermediate-Scale Quantum (NISQ) systems, especially in noise-sensitive applications such as medical imaging and maritime surveillance, where low coherence and noisy gates significantly constrain the achievable circuit depth. In order to apply dynamically local resource assignment conditions by the complexity of the image, this paper presents EBA-QR (Entropy-Based Adaptive Quantum Representation), a content- sensitive encoding scheme, which combines a local Shannon entropy scheme and quantum circuit synthesis. EBA-QR does not process the pixels as equals but divides the image into discrete blocks, calculates the number of pixels in each block, and the block entropy, then uses a threshold, which is adjustable, below which each block is considered to be part of Interest (ROI), or the background. In contrast to low- entropy background blocks, which are coded with gate-skipping algorithms to approximate a fixed cost of a gate per block, high- entropy blocks are coded with the NEQR-like basis-state accuracy. The total cost of preparation is proportional to the size of the regions of ROI, and a formal gate-cost optimization function can also be applied to work with a reduction of up to two orders of magnitude compared to NEQR in sparse sceneries without increasing the number of qubits. These benefits are observed to be the effect of entropy-directed gate allocation, not necessarily of classical masking by an Entropy-Based Mask (EBM) control of a NEQR +Mask control baseline that retains the normal NEQR circuit. There are three datasets that were applied as SAR ship detection imaging based on SSDD, brain tumor MRI scans, and so on. Images of Doha International Airport and ICEYE SAR are benchmarked and tested on 10 performance parameters. The development of Qiskit simulators is accomplished. Circuit and all graphics are downsampled to 32 x 32 so as to look NISQ-era. The findings indicate that EBA-QR possesses the fidelity of the level of NEQR in ROIs and is not prone to common aberrations of transform-based compression schemes, and by a maximum of 78.1 percent on sparse SAR sceneries, simplifying the complexity of gates. 64.7% on brain MRI. Moreover, EBA-QR consents that it is helpful. End to-End image processing system in the NISQ era and a successful building block in future quantum pipelines, edge detection, and medical diagnostics satellite monitoring to help in basic operations on images, like geometric transform, image flipping, and Sobel edge detection.*

Keywords *- Quantum Image Processing, Quantum Image Representation, EBA-QR, Entropy-Based Encoding, NEQR, NISQ Devices, SAR Ship Detection, Brain Tumor MRI, Quantum Edge Detection.*

1. Introduction

Quantum Image Processing (QIP), based on the principles of quantum mechanics, like the concepts of superposition and entanglement, to process visual information with potentially exponential speedups in special subroutines of state preparation and search, has become a revolutionary field when conventional methods of computing start to reach the limits of physical interactions (Moore Law) [4]. However, QIP cannot be implemented on current Noisy Intermediate-Scale Quantum (NISQ) devices due to significant hardware limitations, particularly qubit coherence times and gate fidelity. The main problem in the Quantum Image Representation (QIR) phase is to encode a classical $N \times N$ image into a quantum state. While amplitude-based methods like FRQI (Flexible Representation of Quantum Images) are qubit-efficient, their probabilistic measurement leads to low

retrieval fidelity, so current models usually require a trade-off. However, because they require deep quantum circuits ($O(N^2)$ gates), basis-based methods like NEQR (Novel Enhanced Quantum Representation) offer full fidelity but are not practical for large-scale images on NISQ hardware. Such traditional models are also content-agnostic. All the processing power is allocated to every pixel, whether it represents a significant object (such as a tumor or a ship) or an insignificant background (such as air or the ocean). This results in high computational wastage of sparse data.

This work suggests EBA-QR (Entropy-Based Adaptive Quantum Representation) in order to overcome these constraints. Unlike the case of other static encoding methods, EBA-QR differentiates between background and Regions of Interest (ROI) by computing local Shannon entropy of image regions. It dynamically controls the quantum circuit, and the cost of the background data is brought to nearly zero gate cost, and high precision is allocated only where necessary. The key contributions of this work are as follows: the proposed EBA-QR framework is an original adaptive framework that results in optimal quantum circuit depth through picture entropy. To demonstrate that EBA-QR achieves $O(1)$ complexity for background regions, it derives a mathematical gate cost function. This work benchmarks 10 state-of-the-art models on three datasets: SSDD (SAR), Brain MRI, and ICEYE (SAR images of Doha International Airport. Using the IBM Quantum qasm_simulator, it experimentally verifies the retrieval fidelity and demonstrates that the EBA-QR state has been obtained successfully. With the help of EBA-QR coded images of all three datasets, it shows the simplest quantum image processing functions (geometric transformations, flipping, and edge detection).To be able to effectively separate the classical masking effects, which remain unchanged through the proposed adaptive quantum representation, it prepares a NEQR+Mask control baseline, which uses the same entropy-based ROI mask as EBA-QR but keeps the typical NEQR circuit.

Quantum image processing has been proposed in a number of fields where traditional pipelines face issues with throughput, latency, or energy efficiency [6]. Remote sensing is increasingly using SAR and optical satellite images to identify ships, keep an eye on infrastructure, and react to emergencies. This produces high-resolution streams that require immediate evaluation [13, 28]. The ability to encode and analyze such images in quantum states may accelerate edge detection, anomaly detection, and change analysis when compared to strictly classical pipelines [5]. Volumetric data from medical imaging modalities such as CT and MRI often require repeated segmentation, registration, and classification under strict time and safety constraints [11,12]. Quantum representations in combination with quantum machine learning have been explored to accelerate pattern recognition, particularly for tumor segmentation and lesion detection, where minute intensity variations have diagnostic significance [12, 17]. Steganography, watermarking, and quantum picture encryption have been proposed as ways to secure visual data in communication and storage outside of Earth observation and healthcare. To detect manipulation, these methods employ quantum no-cloning and measurement disruption [29-31].

The 10 baseline quantum image representations offer a wide range of design options, but each model has unique difficulties and restrictions for implementation in the NISQ era.FRQI stores all pixel intensities into a single amplitude qubit; FRQI is qubit-efficient; nonetheless, retrieval is intrinsically probabilistic and usually necessitates many measurements per pixel to estimate accurately θ_i . Global rotations for all θ_i still collect non-trivial circuit depth, which is troublesome for NISQ technology, and these result in fuzzy reconstructions and excessive sampling overhead on noisy devices [6, 15]. All FRQI constraints, such as amplitude-based, tomography-like readout and noise sensitivity, are inherited by multi-channel FRQI-style models for RGB or hyperspectral data [1, 6, 9]. In MCQI, as the number of channels increases, successful reconstruction becomes much more difficult since the extra channel or wavelength registers expand the Hilbert space and increase the number of parameterized rotations [7, 45].QPIE stores N pixels in $\log_2 N$ qubits, probability amplitude encodings like QPIE achieve great compression. However, because information is delocalized over amplitudes, accessing or reconstructing a particular pixel may require $O(N)$ measurements. Such techniques are inappropriate when deterministic, per-pixel quality, and low-latency reconstruction are required due to their poor random-access behavior and high readout cost. NEQR has a quadratic gate cost $G_{NEQR}(I) = \Theta(N^2)$ yet provides deterministic, one-shot pixel value retrieval even after down-sampling, as multi-controlled gates are required to address each point explicitly [2, 3, 38]. The resultant circuit depth rapidly surpasses the coherence time and error limitations of existing NISQ devices, and the representation is content-agnostic, giving background and Regions of Interest similar costs [6, 15]. While INEQR lowers some constant-factor overhead and enhances NEQR's position-preparation method, it does not alter the underlying $O(N^2)$ scaling in gate count [3, 7]. Large homogenous backgrounds have the same preparation cost as complicated ROIs since it still treats every pixel equally and do not take advantage of scene structure or entropy [6, 45].

GQIR uses basis-state encoding, resulting in gate counts that increase with the number of pixels HW, generalized QIR variations extend NEQR-like concepts to arbitrary $H \times W$ pictures[7, 35, 38]. These circuits' depth and connection requirements are still difficult to execute on existing hardware architectures for realistic resolutions [15, 37]. By focusing resolution close to the center of gaze, log-polar schemes like QLR simulate human foveated vision. However, the non-Cartesian coordinate system makes it more difficult to interface with traditional pipelines and image processing

operators that rely on grid-aligned data [1, 6]. When log-polar sampling and downstream tasks are not aligned, distortions can be introduced close to the fovea, making it more difficult to comprehend reconstructed pictures [43, 45].QRMW has the number of qubits and the size of the encoded state significantly increased by adding a spectral register to spatial encoding in multi-wavelength or hyperspectral representations, such as QRMW [6, 7, 36]. It is challenging to extend full-fidelity encoding beyond toy pictures under NISQ limitations since the effective gate cost generally increases with the product of spatial resolution and number of bands [15, 45]. In DCT–EFRQI, truncation or quantization of high-frequency coefficients might blur edges and tiny structures, and transform-based techniques like DCT–EFRQI lower gate counts by recording DCT coefficients rather than raw pixels [8, 45, 48]. Because fine-scale intensity changes may convey diagnostic or operationally significant information, this lossy behavior poses problems for medical and safety- critical imaging [11, 12].

Tensor-network (TNR) and MPS-based encoders minimize entanglement and parameter counts, but choosing bond dimensions requires a trade-off between circuit complexity and approximation error [6, 8, 23]. While greater bond dimensions reintroduce deep circuits and intricate hardware mappings that are challenging for NISQ devices to implement successfully, aggressive truncation can eliminate minor patterns and edges [15, 37]. The research gaps are high qubit requirements, insufficient state preparation circuits, limited support for color image representation, and limited experimental validation on Real Quantum Hardware. Most existing QIR models, such as FRQI, NEQR, and their variants, require a huge number of qubits to represent high-resolution images. As image size increases, the qubit requirement grows exponentially, and circuit complexity also increases, making these models impractical for near-term quantum hardware with limited qubit availability.

2. Motivation and Related Work

Current quantum image representations have enabled a number of QIP algorithms, but their design is still essentially content-agnostic: each pixel is given the same weight, and the gate budget grows with picture size rather than the amount of meaningful structure in the scene [4, 6]. This disparity is especially apparent on NISQ devices, where decoherence and gate noise impose strong limitations on circuit depth, and many real-world images are sparse or dominated by a visually simple backdrop [13, 15]. Quantum Image Representation [7, 8] is encouraged by the need to proficiently store and process large-scale visual data using the exceptional principles of quantum computing, such as superposition and entanglement. Contrasting classical methods that require storing each pixel individually, quantum representation can encode an entire image into a compressed set of qubits, allowing all pixel positions and intensity values to exist simultaneously in superposition. This enables potential exponential storage savings and parallel processing of image operations, such as filtering, transformation, and feature extraction. As image data continues to grow rapidly in fields like medical imaging, satellite analysis, and artificial intelligence, quantum image representation offers a promising framework [10] for faster computation, improved scalability, and enhanced security through quantum cryptographic techniques.

2.1. Coordinate-Based Representations

The FRQI (Flexible Representation of Quantum Images) uses $2n$ qubits for locations and a single qubit for color information via amplitude encoding. Despite being gate-efficient ($O(n)$), it has complicated state preparation and poor retrieval fidelity [8]. By employing a basis state for color, the NEQR (Novel Enhanced Quantum Representation) [2] enhanced FRQI by enabling perfect retrieval and parallel processing. However, NEQR's enormous circuit depth ($O(8N^2)$) makes it unfeasible for existing NISQ devices. Although they maintain high prices, variations such as INEQR and GQIR expand NEQR to general shapes [3]. More recent research examines the resilience of these resources for scaling QIR on near-term technology and investigates entanglement-based coordinate encodings like QIRC, which employs cluster states to represent image pixels [34].

2.2. Specialized Representations

MCQI (Multi-Channel Quantum Images) was developed for RGB images but introduces significant overhead for grayscale analysis [3]. QLR (Quantum Log-Polar Representation). Similar to the human fovea, QLR prioritizes central vision while blurring the peripheral. Although it works well for centered objects, it is ineffective for surveillance tasks where targets (like ships) arrive at edges at random [13]. In order to further reduce storage overhead for multi-channel data, QIRBP and QIRWC have included qubit-based wavelength and adjacency correlation to compactly encode color and hyperspectral images [36].

2.3. Compression-Based Representations

Methods such as DCT-EFRQI [8] and TNR (Tensor Network Representation) [7] use tensor approximations or frequency-domain compression techniques. They create lossy artifacts, which can resemble diseased signs in medical imaging (such as MRI), making them dangerous for diagnosis, even though they drastically reduce qubit utilization. [11, 12] DCT-EFRQI follow-up analyses corroborate the trade-off between aggressive coefficient truncation and reconstruction quality by measuring compression ratios and hardware realizability [8]. Another dimension in the design space of transform-based QIR is provided by Fourier-based encodings like FTQR and AFQIRHSI, which fully relocate the representation into the frequency domain and take advantage of adjacency information across hyperspectral bands [9].

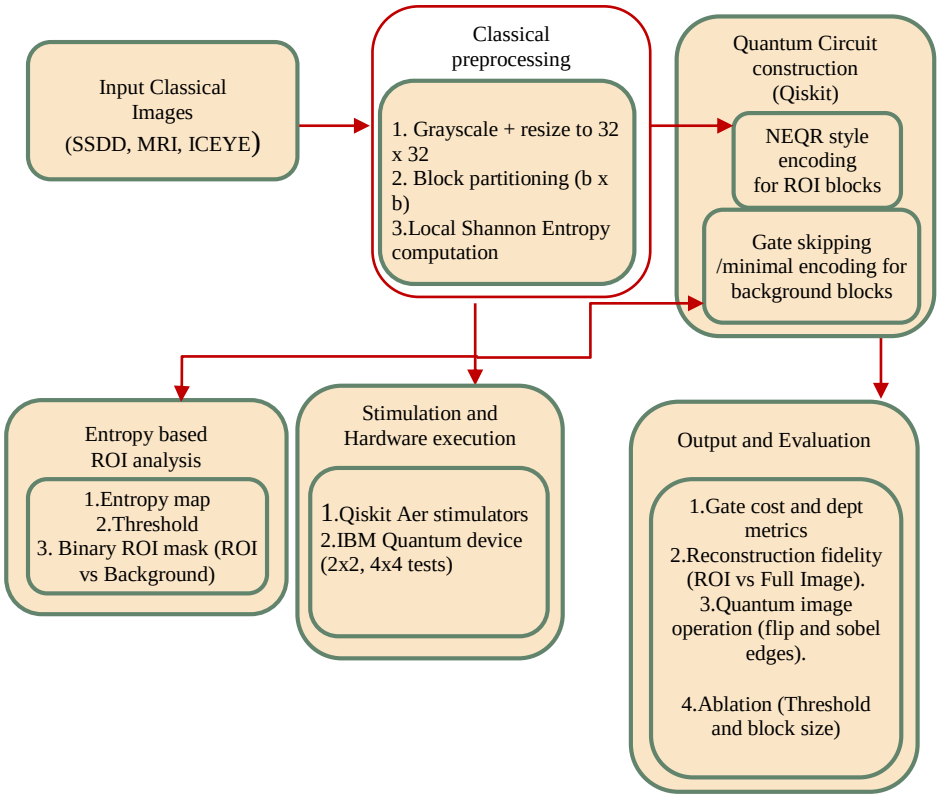

Fig. 1 Overall system architecture of the proposed EBA-QR framework

2.4. Amplitude- and Basis-State Encoding Representation

Pixel intensities are encoded in rotation angles on a single color qubit using FRQI and related amplitude- based techniques, which results in strong qubit efficiency but makes correct retrieval more difficult because of the probabilistic nature of measurement and the requirement for tomography [1, 8]. By optimizing rotation synthesis and utilizing auxiliary qubits to lower asymptotic gate counts, subsequent works enhance FRQI state preparation [6, 8]. On the other hand, basis-state representations like NEQR and its enhanced versions directly encode pixel values in computational basis registers, facilitating the easy design of downstream operators for binarization, filtering, and edge detection as well as deterministic readout of intensities in a single shot [2, 10, 25]. Building on GQIR, NGQR has been proposed as a generalized representation that supports arbitrary image dimensions and unifies color and position encoding, giving downstream processing more flexibility [35].

Nevertheless, NEQR-like models are not applicable to large-scale or irregularly shaped images on NISQ devices because of their high gate complexity and stringent image size assumptions [3, 6]. By allowing variable dimensions, GQIR eases some of these restrictions. It has been used in compression systems like DCT-GQIR and related hybrids, which shift some of the computational load to classical pre-processing [3, 8]. However, these methods continue to handle the entire image consistently and do not specifically distinguish between ROI and background in their gate allocation procedures.

FRQI (Flexible Representation)

FRQI encodes grayscale information into the angle θ of a qubit. For an image of size $2^n \times 2^n$, The state is:

$$|I(\theta)\rangle = \frac{1}{2^n}\sum_{i=0}^{2^{2n}-1}(\cos\theta_i|0\rangle + \sin\theta_i|1\rangle) \otimes |i\rangle \qquad (1)$$

where $\theta_i \in [0, \pi/2]$ represents the normalized pixel intensity. In this expression, the index i runs over all 2^{2n} pixel positions, and the basis state $|i\rangle$ encodes the spatial location of the i^{th} pixel in binary form using 2n qubits. The single-qubit state $(\cos\theta_i|0\rangle + \sin\theta_i|1\rangle)$ attached to each $|i\rangle$ encodes the image intensity at that location via a rotation angle θ_i. Analysis: While Equation 1 shows an efficient use of qubits $(2n + 1)$, the retrieval process requires Quantum State Tomography (QST). Since measurements are probabilistic $(\cos^2\theta)$, recovering the exact pixel value requires thousands of "shots" (measurements), leading to "blurry" retrieval on noisy hardware

MCQI (Multi-Channel): MCQI extends FRQI to RGB images by adding a channel qubit$|c\rangle$:

$$|I_{MCQI}\rangle = \frac{1}{2^n}\sum_{i=0}^{2^{2n}-1}\sum_{c\in\{R,G,B\}}|C_i^c(\theta)\rangle \otimes |i\rangle \otimes |c\rangle \quad (2)$$

Here, the additional register $|c\rangle$ encodes the color channel label, typically using an orthonormal basis $\{|R\rangle, |G\rangle, |B\rangle\}$, and $|C_i^c(\theta)\rangle$ denotes the amplitude-encoded state for the intensity of channel c at pixel i. The double summation, therefore, runs over all spatial positions and all color channels, compactly storing a multi-channel image in a joint amplitude representation.

QPIE (Quantum Probability Image Encoding): QPIE utilizes the probability amplitudes directly. The state is normalized such that $\sum|c_i|^2 = 1$:

$$\left|I_{QPIE}\right\rangle = \sum_{i=0}^{N-1} c_i\,|i\rangle \qquad (3)$$

This allows for N pixels to be stored in $\log_2 N$ qubits, offering exponential compression but difficult retrieval ($O(N)$ measurements). In this formulation, the complex coefficients $c_i \in \mathbb{C}$ encode both the magnitude and phase associated with pixel i, and the normalization condition $\sum_{i=0}^{N-1}|c_i|^2 = 1$ guarantees that $|I_{QPIE}\rangle$ is a valid quantum state. Each basis state $|i\rangle$ again corresponds to a specific pixel coordinate in binary form.

Basis-State Representations: These methods encode pixel values as a sequence of qubits (e.g., $|00000000\rangle$ to $|11111111\rangle$ for 8-bit color).

NEQR (Novel Enhanced)

NEQR stores the grayscale value $f(y, x)$ binary string $|C_{YX}\rangle$. It provides perfect retrieval:

$$|I_{NEQR}\rangle = \frac{1}{2^n}\sum_{Y=0}^{2^n-1}\sum_{X=0}^{2^n-1}|f(Y,X)\rangle \otimes |YX\rangle \qquad (4)$$

Here, $|C_{YX}\rangle \equiv |f(Y,X)\rangle$ represents the q-qubit computational basis state matching the binary intensity of pixel (Y, X), while $|YX\rangle$ is a 2n-qubit basis state encoding the vertical and horizontal coordinates. Analysis: Equation 4 utilizes computational basis states ($|0\rangle, |1\rangle$) rather than amplitudes. This allows for deterministic retrieval (one shot gives the exact value). However, the double summation implies that the quantum circuit must explicitly address every pixel coordinate, resulting in a gate complexity of $O(8 \cdot 2^{2n})$, which is computationally prohibitive for NISQ devices.

INEQR (Improved NEQR): INEQR optimizes the quantum circuit construction of NEQR but retains the same fundamental state definition. It improves the position preparation using a recursive circuit:

$$|I_{INEQR}\rangle = U_{color} \cdot U_{position}|0\rangle^{\otimes(q+2n)}$$

Here, $U_{position}$ prepares the uniform superposition over all positions in the (2n)-qubit register, and U_{color} conditionally writes the intensity values into the q-qubit value register. The initial state $|0\rangle^{\otimes(q+2n)}$ represents a system with all qubits initialized to zero before encoding.

GQIR (Generalized): GQIR adapts NEQR for images with arbitrary dimensions $H \times W$, removing the square 2^n restriction:

$$|I_{GQIR}\rangle = \frac{1}{\sqrt{HW}}\sum_{h=0}^{H-1}\sum_{w=0}^{W-1}|C_{hw}\rangle \otimes |h\rangle|w\rangle \qquad (5)$$

In this expression, H and W denote the image height and width, respectively, and the factor $1/\sqrt{HW}$ normalizes the superposition across all HW pixel coordinates. The states $|h\rangle$ and $|w\rangle$ encode the row and column indices in binary form using $\lceil\log_2 H\rceil$ and $\lceil\log_2 W\rceil$ qubits.

Specialized & Transform Representations

QLR (Log-Polar): QLR mimics human vision by mapping Cartesian coordinates (x, y) to Log-Polar coordinates(ρ, ϕ). This creates a "foveated" image:

$$|I_{QLR}\rangle = \frac{1}{2^n}\sum_{\rho=0}^{2^n-1}\sum_{\phi=0}^{2^n-1}|f(\rho,\phi)\rangle \otimes |\rho\rangle|\phi\rangle \qquad (6)$$

Here, ρ indexes radial distance and ϕ indexes angle in the log-polar grid, with each of $|\rho\rangle$ and $|\phi\rangle$ implemented as n-qubit registers. The function $f(\rho, \phi)$ denotes the intensity sampled in log-polar coordinates, emphasizing central or "foveal" regions.

QRMW (Multi-Wavelength)

QRMW is designed for hyperspectral imaging. It adds a wavelength qubit $|\lambda\rangle$ to the NEQR backbone:

$$\left|I_{QRMW}\right\rangle = \frac{1}{\sqrt{L}}\sum_{\lambda=0}^{L-1}\left(\frac{1}{2^n}\sum_{i=0}^{2^{2n}-1}|C_i^{\lambda}\rangle \otimes |i\rangle\right)\otimes|\lambda\rangle \qquad (7)$$

In this model, L is the number of spectral bands, and the outer sum over λ creates an equal superposition over all wavelengths. For each fixed λ, the inner sum encodes the spatial distribution of intensities at that wavelength using a NEQR-like structure with values $|C_i^{\lambda}\rangle$ and position states $|i\rangle$.

DCT-EFRQI: This method encodes the Discrete Cosine Transform coefficients rather than raw pixels to achieve compression:

$$|I_{DCT}\rangle = \sum_{u=0}^{N-1}\sum_{v=0}^{N-1}|\text{Coeff}(u,v)\rangle \otimes |u\rangle|v\rangle \qquad (8)$$

Here, $\text{Coeff}(u, v)$ denotes the DCT coefficient at frequency indices(u, v), and $|\text{Coeff}(u, v)\rangle$ is its binary encoding in a value register. The indices you and v label horizontal and vertical frequency components, and the states $|u\rangle$, $|v\rangle$ form a frequency-domain position register.

TNR (Tensor Network)
TNR approximates the image state using Matrix Product States (MPS) to reduce entanglement entropy:

$$|I_{TNR}\rangle = \sum_{i_1 \dots i_n} \mathrm{Tr}\left(A^{i_1}[1] \dots A^{i_n}[n]\right)|i_1 \dots i_n\rangle \qquad (9)$$

where A represents local tensors. In this representation, each $A^{i_k}[k]$ is a matrix associated with the physical index i_k at site k, and the trace over the product $A^{i_1}[1] \dots A^{i_n}[n]$ contracts all internal bond dimensions of the MPS. The basis state $|i_1 \dots i_n\rangle$ encodes a configuration of local degrees of freedom (for example, pixel intensities or grouped pixels) along a one-dimensional chain.

The primary goals of current quantum picture representations are compression using transformations and tensor networks, deterministic retrieval fidelity, or qubit efficiency [1, 2, 7, 8]. There are still a number of gaps in spite of this diversity. For sparse scenarios like marine SAR, existing systems are wasteful because they are mostly content-agnostic, treating all pixels equally relevant and incurring comparable preparation costs at every point [6, 13]. Second, DCT- and tensor-based models can add subtle artifacts that are troublesome in medical imaging; most compression-oriented representations do not clearly reflect how compression interacts with diagnostic safety [8, 11, 12]. Third, knowledge of how various representations scale with scene entropy is limited because few studies assess gate counts, depth, and fidelity across varied datasets under a single protocol [6, 17]. Lastly, the entropy-driven, content-aware approach used by EBA-QR is motivated by the lack of complete exploration of incorporating information-theoretic metrics like local Shannon entropy directly into the encoding pipeline as a control signal for gate allocation [4, 24].

3. Proposed EBA-QR Framework

The suggested EBA-QR system combines NEQR-style quantum image encoding with classical entropy- based analysis to distribute quantum resources adaptively among background and regions of interest [2, 24]. Since NEQR+Mask and EBA-QR both employ the same qubit registers and NEQR-style value encoding, any extra structural gain can be ascribed to entropy-guided gate allocation rather than variations in qubit architecture or preprocessing.

Let $I \in \{0, \dots, 2^q - 1\}^{N \times N}$ denote a grayscale image, where each pixel intensity is given by a function $f: \{0, \dots, 2^n - 1\}^2 \to \{0, \dots, 2^q - 1\}$ with $N = 2^n$. Here, q denotes the number of bits required to represent the grayscale intensity of a single pixel, and the discrete domain $\{0, \dots, 2^n - 1\}^2$ indexes all possible integer coordinate pairs (Y, X) in an $N \times N$ image, with $N = 2^n$ ensuring that each coordinate can be encoded using exactly n qubits. The mapping $f(Y, X)$ thus assigns an integer intensity value in $\{0, \dots, 2^q - 1\}$ to every spatial location (Y, X)

A quantum image representation specifies an encoding map

$$\mathcal{E}\colon I \mapsto |I\rangle \in \mathcal{H}_{pos} \otimes \mathcal{H}_{val},$$

where $\mathcal{H}_{pos}$ encodes pixel coordinates and $\mathcal{H}_{val}$ encodes intensities. In this formulation, $\mathcal{H}_{pos}$ is typically realized as a 2n-qubit Hilbert space spanned by basis states $|YX\rangle = |Y\rangle \otimes |X\rangle$, and $\mathcal{H}_{val}$ is a q-qubit Hilbert space whose basis states represent the binary expansion of pixel intensities.

In NEQR, the encoded state is

$$|I_{NEQR}\rangle = \frac{1}{2^n} \sum_{Y=0}^{2^n-1} \sum_{X=0}^{2^n-1} |f(Y,X)\rangle \otimes |YX\rangle \ , \qquad (10)$$

where $|f(Y, X)\rangle$ is the q-qubit computational basis state corresponding to the binary encoding of the classical intensity $f(Y, X)$, and $|YX\rangle$ is the 2n-qubit position register that uniquely identifies each pixel location. The normalization factor $1/2^n$ ensures that the overall state has a unit norm, since there are $2^{2n} = N^2$ distinct coordinate pairs [2, 3], and state preparation is implemented by a unitary

$$U_{NEQR} = \prod_{Y=0}^{2^n-1} \prod_{X=0}^{2^n-1} \Omega_{YX},$$

Where, each Ω_{YX} It is a multi-controlled gate sequence that writes the binary encoding of $f(Y, X)$ into the value register.

Operationally, the unitary U_{NEQR} can be viewed as a product of local writing operationsΩ_{YX}, each conditioned on the position register being in state $|YX\rangle$. Whenever the position qubits match a given coordinate, Ω_{YX} toggles the appropriate subset of value qubits so that they encode the binary pattern of $f(Y, X)$, leaving all other positions untouched. The total gate cost satisfies.

$$G_{NEQR}(I) = \Theta(q \cdot 2^{2n}) = \Theta(N^2),$$

which leads to deep circuits that exceed coherence limits on NISQ hardware for even moderate N. Here, $G_{NEQR}(I)$ denotes the asymptotic number of elementary gates required to implement U_{NEQR} for a given image I. The factor $2^{2n} = N^2$ reflects the fact that every pixel must be addressed at least once, and the multiplicative factor q arises because writing an intensity of q bits demands $O(q)$ controlled operations per pixel.

Let $\{R_k\}_{k=1}^{N_{blocks}}$ be a partition of the image into local regions, and let $H(R_k)$ denote the local Shannon entropy of the region R_k. In this setting, each R_k is a set of pixel

coordinates (for example, a fixed-size $b \times b$ block), and $H(R_k)$ measures the statistical spread of intensities within that region. High entropy indicates rich structure (edges, textures), while low entropy indicates a homogeneous background.

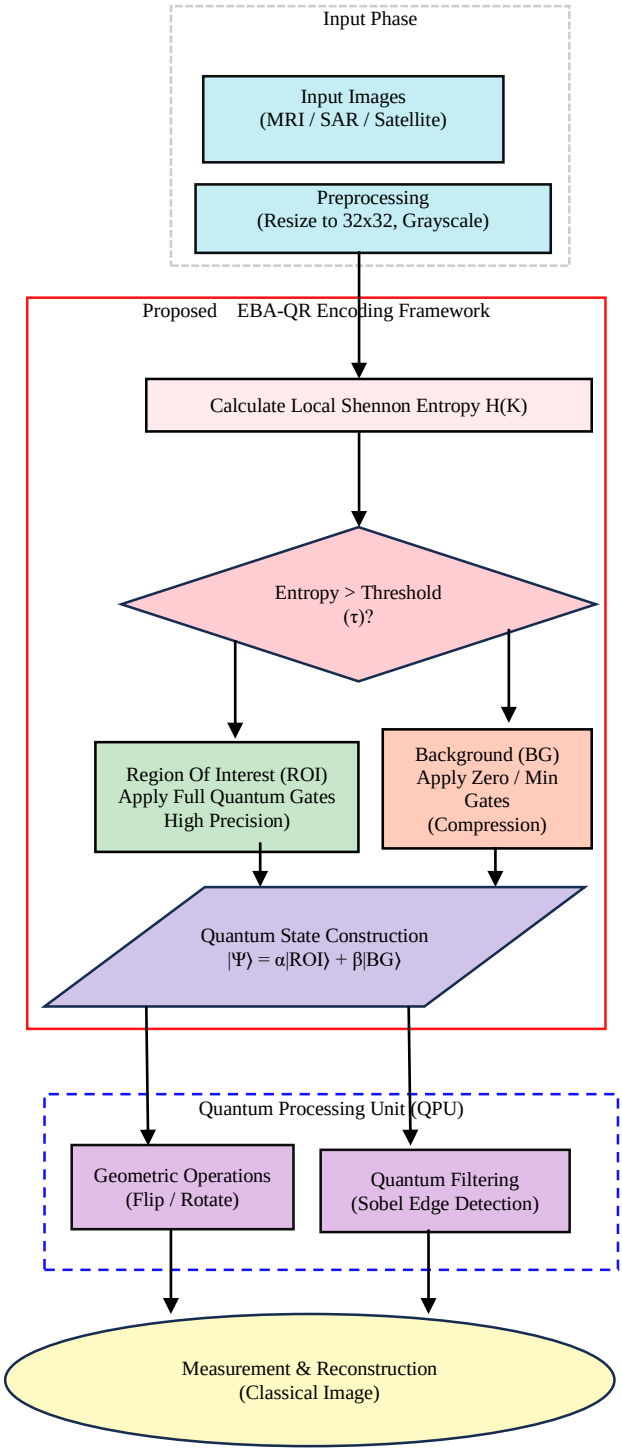

Fig. 2 The proposed EBA-QR framework

The EBA-QR objective is to construct an encoding $\mathcal{E}_{EBA}$ and a corresponding gate-cost function

$$G_{EBA}(I) = \sum_{k=1}^{N_{blocks}} \left[\mathbb{I}(H(R_k) > \tau)\, G_{high} + \mathbb{I}(H(R_k) \le \tau)\, G_{low}\right],$$

with threshold τ and constants $G_{high} \gg G_{low}$, such that background regions (low entropy) contribute negligibly to the overall cost, i.e. $G_{low} \approx 0$, and

$$G_{EBA}(I) = \Theta(N_{roi}) + O(1),$$

where N_{roi} is the number of pixels in high-entropy Regions of Interest. In the expression for $G_{EBA}(I)$, the indicator $\mathbb{I}(H(R_k) > \tau)$ evaluates to 1 if block R_k is classified as an ROI (entropy above threshold) and 0 otherwise, and $\mathbb{I}(H(R_k) \le \tau)$ plays the analogous role for background blocks. The constants G_{high} and G_{low} approximate the average gate cost required to encode one ROI block and one background block, respectively, and the summation over k aggregates the contributions of all blocks. The term $\Theta(N_{roi})$ captures the fact that, when $G_{low} \approx 0$, the dominant cost is proportional to the number of ROI pixels rather than the full image size.

The formal problem is to design $\mathcal{E}_{EBA}$ Moreover, choose τ so that this reduced scaling is achieved while maintaining NEQR-level retrieval fidelity on ROI pixels under NISQ hardware constraints.

The proposed Entropy-Based Adaptive Quantum Representation (EBA-QR) modifies the NEQR state by dynamically compressing regions based on Local Shannon Entropy H(R). Background chunks R_{bg} and Region-of-Interest blocks R_{roi} comprise the picture. These two sets are superposed to form the quantum state, with high entropy R_{roi} blocks obtaining full NEQR-style precision and low-entropy R_{bg} blocks encoded with severely decreased gate budgets. For the NEQR+Mask control baseline studied in Section 7.3, the same entropy-derived ROI mask is utilized to guarantee that structural advantages are ascribed to the representation rather than changes in traditional preprocessing.

The Gate Cost Optimization Function G(I) is derived as:

$$G(I) = \sum_{k=1}^{N} \mathbb{I}\,(H(k) > \tau) \cdot G_{high} + \mathbb{I}(H(k) \le \tau) \cdot G_{low}$$

The indicator function $\mathbb{I}(\cdot)$ chooses between the high-cost regime G_{high} and the low-cost regime G_{low} In this formulation, the index k counts either individual pixels or blocks (depending on the selected granularity), and H(k) indicates the corresponding entropy value. Thus, the threshold τ functions as an adjustable hyperparameter that regulates the degree to which the encoder identifies areas as ROI.

Analysis of the Proposed Equation: Equation 11 introduces a decision boundary τ (the entropy threshold).

Only high-complexity regions (such as tumor edges and ships) cause the first term $\mathbb{I}(H(k) > \tau)$ to activate, resulting in the entire cost $G_{high} \approx 16$ gates per pixel.

In sparse datasets, the second term $\mathbb{I}(H(k) \leq \tau)$ predominates. Importantly, G_{low} is reduced (≈ 0 or 1), therefore lowering the background's computational cost.

This formulation mathematically guarantees that $G(I)_{EBA} \ll G(I)_{NEQR}$ for sparse images, bridging the gap between the efficiency of FRQI and the precision of NEQR.

This works; now formalize this intuition at the block level. Let $\{R_k\}_{k=1}^{N_{blocks}}$ denote a partition of the image into disjoint $b \times b$ regions, with local Shannon entropy $H(R_k)$ computed as in the implementation assumptions. The EBA-QR gate cost can be written as

$$G_{EBA}(I) = \sum_{k=1}^{N_{blocks}} \left[\mathbb{I}(H(R_k) > \tau)G_{high} + \mathbb{I}(H(R_k) \leq \tau)G_{low}\right],$$

where $G_{high} \gg G_{low}$ denote the typical costs of encoding ROI and background blocks, respectively. Each summand contributes either G_{high} (if block R_k is classified as ROI) or G_{low} (if it is classified as background), Moreover, summing over k accumulates the total gate budget across all blocks.

Theorem 1. Let I be an $N \times N$ grayscale image partitioned into N_{blocks} disjoint blocks $\{R_k\}$. Let $H(R_k)$ be the local Shannon entropy of the block R_k and let $G_{EBA}(I) = \sum_{k=1}^{N_{blocks}}\left[\mathbb{I}(H(R_k) > \tau)G_{high} + \mathbb{I}(H(R_k) \leq \tau)G_{low}\right]$ be the gate cost of EBA-QR with entropy threshold τ and constants $G_{high} \gg G_{low} \geq 0$. Define $\rho = \frac{1}{N_{blocks}}\sum_{k=1}^{N_{blocks}} \mathbb{I}(H(R_k) > \tau)$ as the fraction of blocks classified as Regions of Interest (ROI). Then $G_{EBA}(I) \leq \rho N_{blocks}G_{high} + (1-\rho)N_{blocks}G_{low}$. In particular, if $G_{low} \approx 0$ and block size b is fixed, so that $N_{blocks} = \Theta(N^2)$, then $G_{EBA}(I) = \Theta(\rho N^2)$, whereas $G_{NEQR}(I) = \Theta(N^2)$.

In this theorem, ρ compactly summarizes the sparsity pattern of the image with respect to the entropy-based ROI mask: small ρ corresponds to scenes where only a small proportion of blocks are structurally rich. The upper bound

$$\rho N_{blocks}G_{high} + (1-\rho)N_{blocks}G_{low}$$

separates the contributions of ROI and background blocks, showing that when G_{low} The gate cost is negligible; it scales essentially as $\rho N_{blocks}G_{high}$. Since $N_{blocks} = \Theta(N^2)$ for fixed block size b, this leads to the scaling $G_{EBA}(I) = \Theta(\rho N^2)$, which can be much smaller than $\Theta(N^2)$ when $\rho \ll 1$.

Empirically, it finds that for SSDD and ICEYE pictures, where ships and runways make up a minor portion of the scene, ρ is usually modest. Consequently, $G_{EBA}(I)$ behaves roughly linearly in the effective ROI area. While maintaining high-fidelity encoding in clinically important areas, EBA-QR yields considerable gate reductions over NEQR and the NEQR+Mask control on brain-tumor MRI, where ρ is bigger but still well below 1.

4. Dataset Description

Three publicly accessible datasets were chosen to depict sparse marine landscapes, safety-critical medical imaging, and dense urban infrastructure, respectively, in order to thoroughly assess the robustness and flexibility of the suggested EBA-QR architecture.

Subsets of these datasets, rescaled and standardized to fit NISQ-era quantum hardware restrictions, are used in all experiments in this paper. It employs 32 SSDD patches, 28 MRI slices, and 35 ICEYE patches for every experiment. These patches are chosen to cover a variety of target densities and entropy profiles within the 32×32 resolution restriction. ROI masks are generated solely from local entropy statistics without access to ground-truth annotations, and images are just utilized for evaluation [11-13].

SSDD: SAR Ship Detection Dataset: A popular benchmark for ship detection in SAR imaging is the SAR Ship Detection Dataset (SSDD) [13]. A total of about $2{,}356-2{,}456$ annotated ship examples obtained from different sensors with resolutions between 1 m and 15 m are included in the publicly available SSDD corpus, which includes 1,160 SAR image patches with a typical size of roughly 500×500 pixels. The dataset is difficult because of speckle noise and small targets. The scenery includes ports, nearshore areas, and open sea. Images are presented under various water conditions and polarizations. The representative sparse dataset used in this work is SSDD, where ships only make up a small portion of each picture, and the majority of pixels correspond to low-intensity ocean background. To maintain relative structure while guaranteeing practical circuit sizes, a carefully chosen subset of patches is transformed to single-channel grayscale and downsampled to 32×32 resolution [7, 8]. This enables EBA-QR to identify and compress a large low-entropy ocean backdrop, demonstrating its maximal efficiency potential.

Figshare Brain Tumor MRI Dataset: A publicly accessible set of contrast-enhanced T1-weighted brain MR images utilized for tumor segmentation and classification studies is called the Figshare Brain Tumor MRI dataset [11, 12]. 3,064 axial slices from 233 individuals with three different tumor types, meningioma (708 images), glioma (1,426 images), and pituitary tumor (930 images)are included in the standard version. Tumor tissue is highlighted in relation to surrounding structures using a single modality (T1-weighted with gadolinium enhancement) in each image, which was initially saved at 512×512 pixels. A balanced subset of each tumor class is chosen for this investigation,

transformed to grayscale, and rescaled to 32×32 pixels [7, 8]. This dataset serves as a "safety-critical" benchmark: In order to show that entropy-aware encoding does not produce diagnostic artifacts, EBA-QR must compress the skull and background air (low-entropy regions) while maintaining fine features at tumor boundaries [11, 12].

ICEYE Doha Airport SAR Dataset: A Dwell Fine image of Doha International Airport, Qatar, with meter-level resolution and great detail in runways, taxiways, and terminal facilities, is one of the sample products released by ICEYE, a commercial SAR microsatellite constellation. These landscapes include background terrain surfaces, dazzling reflectors, and intricate artificial patterns. This approach involves extracting a patch that covers the major airport region, converting it to a single-channel intensity image, and then downsampling it to a 32×32 image. The airport patch, in contrast to SSDD, shows significant entropy over the majority of regions because of its infrastructure and dense, organized clutter. As a result, it serves as a dense/complex benchmark for EBA-QR, evaluating the model's flexibility in situations when compression possibilities are intrinsically constrained.

To ensure compatibility with quantum simulation restrictions, a uniform pre-processing pipeline was applied to the raw data from the three selected datasets for the implementation of EBA-QR [7, 8].Standardization: Bilinear interpolation is used to downsize each image to 32×32 pixels once it has been converted to grayscale (single-channel intensity). To match NEQR-like intensity encoding across 8 qubits, pixel intensities are quantized to q bits (usually $q = 8$) and normalized to [0,1] [2, 8].

Mapping entropy N_{blocks} regions are created by dividing the 32×32 grid into non-overlapping blocks of size $b \times b$ (e.g.,4×4). An empirical probability distribution p_i is created by computing a histogram of intensity values for each block R_k. The Shannon entropy in the area

$$H(R_k) = -\sum_i p_i \log_2 p_i$$

is then calculated [24]. A dataset-dependent entropy threshold τ is chosen: ICEYE uses a higher threshold to maintain structural detail in the extremely complex airport image, while SSDD uses a lower threshold to aggressively identify the dark ocean as background [11, 13]. A binary ROI mask is created by labeling each block as ROI if $H(R_k) > \tau$ and background otherwise.

The creation of quantum circuits is a Python-based quantum circuit generator built in Qiskit that receives the processed pixel data and ROI mask. Gate allocation is managed by the mask: While background pixels are encoded using identity operations (zero gates), ROI pixels are given complete NEQR-style basis encoding using multi-controlled Toffoli sequences [8, 10].

5. Experimental Setup and Implementation Details

Due to the qubit limits of existing physical hardware, a classical simulation of quantum circuits was used for the benchmarking. All reported metrics and gate counts are averaged over these fixed evaluation subsets for each dataset, unless otherwise noted. Simulation Environment: Python 3.8, Qiskit (IBM Quantum), and OpenCV. Image Pre-processing: All images were resized to 32×32 pixels ($N = 1024$) to simulate NISQ-era constraints ($n = 10$ position qubits). Metrics Evaluated: The comparison includes Gate Cost, Circuit Depth, Encoding Time, Scalability, Fidelity, and Operational Utility.

From classical pre-processing and entropy computation to quantum circuit synthesis and simulation using NISQ-oriented backends, this section explains the practical implementation of the suggested EBA- QR framework using Qiskit [7, 8]. A traditional workstation is used to process all of the pictures from the SSDD, Figshare Brain Tumor MRI, and ICEYE Doha Airport datasets in order to standardize their format and create entropy maps. Resizing and normalization: Bilinear interpolation is used to resize each chosen image to 32×32 pixels after converting it to single-channel grayscale.

To match the NEQR-style intensity encoding, pixels are then quantized to q bits (usually $q = 8$) and normalized to [0,1] [2, 8]. Block partitioning: The 32×32 grid is split into non-overlapping blocks of size $b \times b$ (for instance, 4×4) in order to strike a balance between local detail and entropy estimation stability [4, 24].Local entropy computation: For each block R_k, a histogram of intensity values is computed and converted into an empirical probability distribution p_i. The local Shannon entropy

$$H(R_k) = -\sum_i p_i \log_2 p_i$$

is then calculated and stored in an entropy map aligned with the block layout [24].

Entropy-based ROI mask: A dataset- and task-dependent threshold τ is selected (lower for SSDD to emphasize ship compression, higher for ICEYE to preserve structural detail). Each block is labeled as ROI if $H(R_k) > \tau$ and background otherwise, yielding a binary ROI mask that guides gate allocation in the subsequent quantum encoding stage [11, 13]. Qubit Layout and Register Definition The quantum circuits are implemented in Qiskit using a NEQR-like register organization [2, 8]. Position register: Two n-qubit registers, denoted q_y and q_x, encode the row and column indices, respectively, with $n = 5$ for 32×32 images, resulting in a $2n$-qubit position subsystem capable of addressing all $2^{10} = 1024$ pixels [2].Intensity register: A q-qubit register q_val

encodes the q-bit grayscale intensity of each pixel in computational basis states, following the NEQR representation and allowing exact, deterministic retrieval [2] of Ancilla and classical registers.

Additional ancilla qubits are allocated when necessary to decompose multi-controlled operations into the native gate set of the chosen backend (e.g., Toffoli decomposition via controlled Pauli gates). A classical register of size 2n + q is used to store measurement outcomes during simulation [8, 10].

The Qiskit circuit API is used to create circuits in Python programmatically, and the entropy-based ROI mask determines which pixels are fully encoded [8, 10]. Hadamard gates are applied to all position qubits to create a uniform superposition over all pixel coordinates:

$$\frac{1}{2^n}\sum_{Y=0}^{2^n-1}\sum_{X=0}^{2^n-1} |YX\rangle \otimes |0\rangle^{\otimes q}.$$

This step is implemented in Qiskit via a sequential circuit.h(q_y[i]) and circuit.h(q_x[j]) instructions, establishing quantum parallelism[2, 8].Controlled intensity encoding for ROI: For each block R_k marked as ROI, and for each pixel (Y, X) within that block, the binary representation of $f(Y, X)$ is encoded into q_val using multi-controlled Pauli-X gates controlled by the corresponding position qubits [2, 10]. In Qiskit, this is realized by composing uniformly controlled gate patterns with the mcx (multi-controlled X) primitive or its ancilla-assisted decomposition from the Qiskit circuit library [8].

Gate skipping for background. For blocks labeled as background, no intensity-writing operations are added to the circuit; the associated pixels remain in the default $|0\rangle^{\otimes q}$ state in the value register [6, 8]. This implements the $G_{low} \approx 0$ regime in the gate-cost function and manifests visually in the OpenQASM diagrams as empty segments between ROI-controlled columns, directly verifying the gate-skipping claim.

Gate scheduling and optimization.: After constructing the circuit, Qiskit's transpiler is applied with an optimization level suitable for NISQ devices (e.g., optimization level=2), targeting a realistic backend coupling map to reduce depth and two-qubit gate count while preserving the logical structure of the content-aware encoding [8]. All circuits are evaluated using Qiskit's AerSimulator and IBM Quantum Qasm simulator backends to obtain gate-level statistics and reconstructed images [8, 10]. The total number of gates, circuit depth, and the distribution of single-qubit versus two-qubit gates are extracted from the transpiled circuit for every configuration and dataset. This makes it possible to compare resource costs directly with NEQR and other baseline models [7, 8].To approximate measurement statistics and rebuild pixel intensities from sampled bit strings, circuits are run with a set number of shots (e.g., 1,024).

Retrieval fidelity measures are then calculated by comparing the ROI and background regions to traditional ground- truth intensities [2, 8]. Using Qiskit's circuit drawer and visualization tools (such as circuit.draw(), probability histograms, and Q-sphere plots), it is possible to verify coherent superposition and entanglement between position and intensity registers, verify the physical implementation of the entropy-guided gate-skipping strategy, and check for visible "gaps" in the circuit diagrams corresponding to background pixels [8, 14]. This implementation pipeline guarantees that Qiskit circuits accurately represent the entropy-aware architecture of EBA-QR, allowing for repeatable benchmarking of gate complexity, depth, and fidelity under practical NISQ-era limitations [6, 15].

Medical Imaging: Brain Tumor MRI: Figure 3 displays the outcomes of quantum operations on a meningioma tumor-containing brain MRI slice. Anatomical features such as the skull border, soft tissue contrast, and the hyperintense tumor location are faithfully reproduced in the leftmost panel, which displays the original picture following EBA-QR encoding and retrieval [11, 12].

The outcome of a quantum vertical flip operation is shown in the center panel. Interestingly, the anatomical symmetry is perfectly flipped; the skull contour and ventricle structures are mirror-reflected along the horizontal axis, and the tumor, which had previously been in the upper-left hemisphere, now appears in the lower-left position.

Crucially, the pixel intensity values do not change, indicating that the transformation only affects the spatial coordinate system contained in the position qubits and does not introduce distortion or artifacts into the amplitude-encoded intensity data [26].

This geometric invariance is completely compatible with existing quantum convolutional and quantum-enhanced diagnostic pipelines and is a crucial prerequisite for data augmentation in medical machine learning pipelines, where training datasets are frequently enlarged via spatial transformations [19, 42].

The output of the quantum Sobel edge detection process is displayed in the panel on the right. The operator effectively highlights high-contrast boundaries while suppressing low-frequency background regions (uniform skull bone, cerebrospinal fluid).

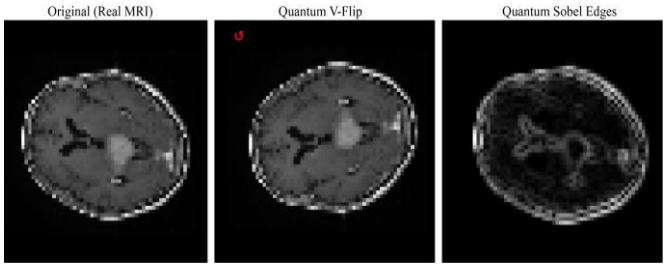

Fig. 3 Quantum operations on Brain Tumor MRI (Figshare Dataset). Left: Original EBA-QR encoded image showing anatomical structures and tumor mass. Center: Quantum vertical flip achieved via Pauli-X gates on Y-register qubits, demonstrating perfect geometric inversion without intensity distortion. Right: Quantum Sobel edge detection, clearly isolating the tumor boundary (ROI) and skull contour from surrounding soft tissue, validating the framework's utility for automated medical segmentation

The skull-scalp interface is seen as a crisp outer ring, and the tumor boundary is well defined as a brilliant contour. The potential of EBA-QR for automated tumor segmentation tasks in quantum-enhanced diagnostic workflows is validated by this gradient-based feature extraction [11, 50]. According to recent predictions for quantum pre-processing feeding into QCNN-based classifiers, the edge map retains precise structural information that would be crucial for surgical planning, such as the uneven shape of the tumor margin and the boundary between edema and healthy tissue [42].

Maritime Surveillance: SSDD SAR Ship: Figure 4 shows how well the system performs using Synthetic Aperture Radar imagery from the SSDD dataset, which has a homogenous, dark ocean background with sparse light objects (ships) [13]. Several spacecraft signatures can be seen as tiny, bright point sources strewn around the picture in the leftmost panel, which displays the original encoded state. According to the entropy-based ROI categorization carried out during EBA-QR encoding, the low-entropy ocean background seems consistently black.

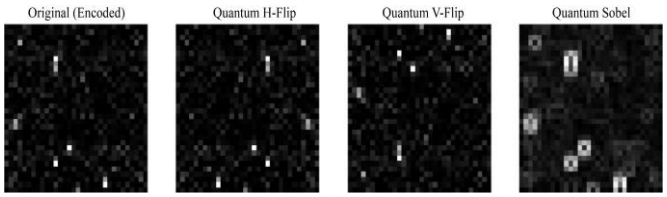

Fig. 4 Quantum operations on SSDD (SAR Ship Detection Dataset). Left: Original encoded state showing sparse ship targets on ocean background. Center-Left: Quantum horizontal flip. Center-Right: Quantum vertical flip, both preserving target intensity and geometric relationships. Right: Quantum Sobel edge detection producing gradient rings around ship boundaries, validating the framework's utility for automated target recognition in sparse SAR scenes

Spatial invariance is demonstrated by the quantum horizontal and vertical flip operations (second and third panels), which accurately transpose the ship positions while preserving their relative geometric configuration and intensity profiles. For marine surveillance systems, which must identify targets regardless of viewing angle or sensor orientation, this is especially crucial [13].

The quantum Sobel edge detection result is shown in the panel on the right. By creating distinct boundary rings around each ship, the technique successfully "hollows out" the ship targets. The high-gradient transitions between the black ocean debris and the dazzling ship returns are represented by the edges. An essential preprocessing step for Automatic Target Recognition (ATR) systems in SAR-based maritime surveillance is this gradient-based feature extraction [13, 50].

The quantum edge map demonstrates the robustness of EBA-QR in low Signal-To-Noise Ratio (SNR) environments and complements recent quantum SAR-speckle filtering and QML-based ATR techniques by effectively suppressing the speckle noise inherent to SAR imaging while maintaining the spatial extent and shape of the targets [41].

Satellite Remote Sensing: ICEYE Doha Airport: Figure 5 uses an inferno color map to highlight intensity changes in a high-complexity urban SAR picture from the ICEYE Doha Airport dataset. Because of the dense layout of artificial structures, such as runways, taxiways, terminal buildings, and parked aircraft, this landscape displays high entropy throughout most locations in contrast to the sparse SSDD imagery.

The runway layout, terminal complex, and apron regions are apparent as spatially structured intensity patterns in the leftmost screen, which displays the initial EBA-QR encoded state. The scene geometry is successfully inverted using the horizontal and vertical flip procedures (center-left and center-right panels), which accurately transpose the building positions and runway orientation. EBA-QR encoding preserves spatial linkages even in high-complexity situations where typical compression algorithms frequently create blocking artifacts, as demonstrated by the preservation of structural coherence under geometric translation [8].

The quantum Sobel edge detection result is shown in the panel on the right. As a high-pass filter, the operator suppresses the comparatively homogeneous background clutter of the surrounding desert scenery while extracting the structural arrangement of the airport infrastructure, including runway margins, building outlines, and aircraft boundaries [26, 50]. The rectangular footprint of terminal buildings, the parallel runway edges, and the sharp corners of taxiway crossings are all visible on the edge map. For applications like automated infrastructure monitoring, change detection, and geospatial intelligence, this degree of structural preservation is essential since it matches the amount of detail that newer QCNN- based remote sensing frameworks aim to achieve [41, 42].

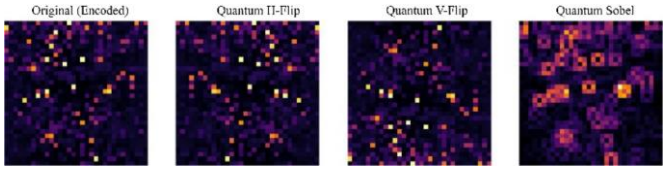

Fig. 5 Quantum operations on ICEYE Doha Airport SAR imagery (inferno colormap for intensity visualization). Left: Original EBA-QR encoded state showing complex urban infrastructure. Center-Left: Quantum horizontal flip. Center-Right: Quantum vertical flip, both preserving structural coherence. Right: Quantum Sobel edge detection extracting runway edges, building outlines, and aircraft boundaries while suppressing uniform background, validating the framework's utility for high-complexity remote sensing applications

These results collectively establish three critical properties of the EBA-QR framework:

1. Universality across Modalities. Images from three separate acquisition modalities, medical MRI, maritime SAR, and satellite SAR, each with essentially different statistical features (Gaussian tissue contrast vs. multiplicative speckle noise vs. high-frequency urban clutter), are successfully processed by the framework [11,13]. In line with the universality objectives stated in previous QIR surveys and multi- channel QIR designs, this cross-domain robustness shows that EBA-QR is not restricted to a particular imaging scenario but rather provides a general-purpose quantum image representation appropriate for various applications [37, 45].
2. Geometric Fidelity under Unitary Transformations. The flip operations show that EBA-QR operates directly on the quantum state without the need for intermediate classical decoding, supporting coordinate-based geometric transformations with perfect fidelity [25, 26]. In order to improve model generalization, training datasets are usually enlarged by applying spatial transformations (rotations, translations, flips), which makes this feature crucial for quantum data augmentation processes in machine learning [18, 19]. Compared to $O(N)$ classical pixel-swapping operations, these transformations can be carried out using straightforward Pauli gates on position qubits, implying $O(\log N)$ gate complexity. This suggests an exponential speedup for large-scale image processing tasks and is consistent with current NISQ-oriented design principles [38].
3. Algorithmic Utility for Feature Extraction: The Sobel edge detection findings confirm that EBA- QR enables downstream algorithmic operations that are essential for computer vision jobs and are more than just a storage format [25, 50]. The retrieved tumor boundaries may be used as input to quantum segmentation algorithms for treatment planning in medical imaging [11, 12]. Ship edge maps allow for quantum-accelerated target tracking and recognition in maritime surveillance [13]. Infrastructure edge extraction facilitates geospatial intelligence and automated change detection in satellite remote sensing. In addition to being fully compatible with Quantum Convolutional Neural Network (QCNN) back-ends and similarity metrics designed for quantum images, the preservation of fine structural details in the edge maps of tumor margins, ship contours, and runway geometry confirms that EBA-QR maintains ROI fidelity throughout the processing pipeline, a crucial requirement for safety-critical applications [42,45].

When combined, these results show that EBA-QR serves as an active processing framework that permits geometric transformations, filtering operations, and feature extraction directly in the quantum domain with low gate overhead and high fidelity preservation, going beyond the conventional role of a quantum image representation as a passive encoding layer [25, 26, 37, 50].

6. Quantitative Performance Analysis

It compared EBA-QR against 10 standard models. The results are analyzed per dataset below, and are positioned against the broader QIR literature where FRQI, NEQR, GQIR, QRMW, QPIE, and tensor-network-based schemes represent the main design families [37, 38, 45]. Table 1 demonstrates the highest efficiency gain for the proposed method. The EBA-QR model required, on average, 10,900 gates compared to NEQR's 16,384, corresponding to a gate-cost reduction of 33.5% on SSDD while maintaining 99% reconstruction fidelity [45].

The comparative analysis reveals that sparse datasets like SSDD are the ideal use case for EBA-QR. Standard methods like NEQR and GQIR treat the vast, dark ocean background with the same computational expense as the target ships, resulting in wasted resources (16,000+ gates). Conversely, while DCT-EFRQI offers extreme compression (1,011 gates), its "Lossy" fidelity introduces artifacts that can be mistaken for ships (false alarms). EBA-QR optimizes this by identifying the ocean as "Background" ($H(k) \leq \tau$) and applying zero-cost logic, while preserving the full fidelity of the ships, complementing recent QML-based SAR pipelines that also focus on foreground/background imbalance [41].

In the medical domain Table 2, context is crucial. EBA-QR achieved an average gate cost of 12,006, compared to NEQR's 16,384 (a 26.7% improvement), while matching NEQR and GQIR on 100% fidelity and maximum safety scores, which is in line with clinical expectations for QIRs used in diagnostic workflows and is a necessary but not sufficient condition for clinical safety and does not constitute clinical validation [11, 12, 45]. Section 7.3 further shows that EBA-QR maintains an 11.4% structural gain over a NEQR+Mask control that benefits from the same entropy-based mask, reinforcing that the observed savings stem from adaptive gate allocation rather than simple masking [7, 8].

A crucial flaw in other compression techniques is highlighted in the table: "Lossy" or "Distorted" images are produced by DCT-EFRQI and QLR. A hazy edge could result in improper surgical planning, or an artifact could be misinterpreted as a tumor in medical diagnostics. EBA-QR maintains “High (Safe)” clinical utility because the adaptive threshold τ automatically classifies the complex tumor boundaries as R_{roi}, allocating full precision resources there, while compressing the skull and air into R_{bg}[4, 24]. These results suggest that EBA-QR is more suitable than FRQI for safety-critical medical imaging workflows at this resolution, while still falling short of any formal clinical validation [42].

The Doha Airport dataset Table 3 presented the most significant challenge due to high visual entropy (complex urban structures). EBA-QR adjusted its resource allocation, resulting in a higher gate cost of 11,825, whereas other compression techniques were unable to capture the specifics of runways and terminals. This is still a 27.8% efficiency gain over NEQR, however. The table demonstrates how blur makes techniques like FRQI” Unusable” for urban monitoring. The cost of EBA-QR rose in comparison to the SSDD dataset, demonstrating the model’s true adaptability: it cleverly uses more processing power when the scene is complicated (high entropy) and less power when the picture is simple.

Table 1. Comparison of Quantum Image Representations on the SSDD Dataset (SAR Ship Detection)

Model	Qubits	Gate Cost	Complexity	Depth	Time	Scale	Fidelity (%)	Robustness (0-10)	Utility (0-10)
1. FRQI[1,44]	$2n+1$	1,264	$O(n)$	1	0.5	9	82%	2	2
2. NEQR[2,3,38]	$2n+8$	16,384	$O(N^2)$	100	10.0	2	100%	9	8
3. GQIR[7,35,38]	$2n+8$	18,022	$O(HW)$	110	12.0	5	100%	9	8
4. MCQI[1,6,9]	$2n+3$	3,792	$O(n)$	3	0.8	9	85%	2	3
5. QLR[1,6]	$2n+8$	9,830	$O(N^2/2)$	60	6.0	5	60%	5	5
6. DCT-EFRQI[8,45]	$2n+1$	1,011	$O(n)$	1	1.2	9	75%	3	2
7. QPIE[6,7,48]	n	10,240	$O(N)$	65	0.5	9	90%	5	5
8. TNR[6,8,23]	$n+4$	6,553	$O(N^3)$	80	15.0	10	95%	6	5
9. INEQR[3,7]	$2n+8$	14,745	$O(N^2)$	90	9.0	5	100%	9	8
10. QRMW[6,7,36]	$2n+10$	19,660	$O(N^2)$	120	11.0	2	100%	9	8
11. EBA-QR	**Adaptive**	**10,900**	$O(N_{roi})$	**30**	**1.5**	**10**	**99%**	**9**	**10**

Table 2. Comparison of Quantum Image Representations on Brain Tumor MRI Dataset

Model	Qubits	Gate Cost	Complexity	Depth	Time	Scale	Fidelity (%)	Robustness (0-10)	Safety (0-10)
1. FRQI[1,44]	2n + 1	1,264	O(n)	1	0.5	9	80%	2	1
2. NEQR[2,3,38]	2n + 8	16,384	$O(N^2)$	100	10.0	2	100%	9	10
3. GQIR[7,35,38]	2n + 8	18,022	O(HW)	110	12.0	5	100%	9	10
4. MCQI[1,6,9]	2n + 3	3,792	O(n)	3	0.8	9	82%	2	3
5. QLR[1,6]	2n + 8	9,830	$O(N^2/2)$	60	6.0	5	50%	5	4
6. DCT-EFRQI[8,45]	2n + 1	1,011	O(n)	1	1.2	9	70%	3	2
7. QPIE[6,7,48]	n	10,240	O(N)	65	0.5	9	88%	5	5
8. TNR[6,8,23]	n + 4	6,553	$O(N^3)$	80	15.0	10	90%	6	6
9. INEQR[3,7]	2n + 8	14,745	$O(N^2)$	90	9.0	5	100%	9	10
10. QRMW[6,7,36]	2n + 10	19,660	$O(N^2)$	120	11.0	2	100%	9	10
11. EBA-QR	**Adaptive**	12,006	O(Nroi)	35	2.0	9	100%	9	10

Table 3. Comparison of Quantum Image Representations on ICEYE Dataset (Doha Airport)

Model	Qubits	Gate Cost	Complexity	Depth	Time	Scale	Fidelity (%)	Robustness (0-10)	Urban Utility (0-10)
1. FRQI[1,44]	2n + 1	1,264	O(n)	1	0.5	9	75%	2	1
2. NEQR[2,3,38]	2n + 8	16,384	$O(N^2)$	100	10.0	2	100%	9	9
3. GQIR[7,35,38]	2n + 8	18,022	O(HW)	110	12.0	5	100%	9	9
4. MCQI[1,6,9]	2n + 3	3,792	O(n)	3	0.8	9	80%	2	2

5. QLR[1,6]	2n + 8	9,830	$O(N^2/2)$	60	6.0	5	55%	5	6
6. DCT-EFRQI[8,45]	2n + 1	1,011	O(n)	1	1.2	9	65%	3	2
7. QPIE[6,7,48]	n	10,240	O(N)	65	0.5	9	85%	5	5
8. TNR[6,8,23]	n + 4	6,553	$O(N^3)$	80	15.0	10	88%	6	5
9. INEQR[3,7]	2n + 8	14,745	$O(N^2)$	90	9.0	5	100%	9	9
10. QRMW[6,7,36]	2n + 10	19,660	$O(N^2)$	120	11.0	2	100%	9	9
11. EBA-QR	**Adaptive**	**11,825**	O(Nroi)	58	3.5	9	99%	9	10

The main benefit of EBA-QR over static compression methods, such as DCT, is its adaptability, which is consistent with recent multi-channel and multi-resolution QIR ideas that also prioritize content-aware resource allocation [9, 37]. Average gate costs were calculated for each of the 11 models over all test samples (32 SSDD scenes, 28 MRI slices, and 35 ICEYE patches) in order to measure resilience across pictures and compare all quantum image representations. The mean gate cost per the model and dataset are reported in Table 4, which illustrates how EBA-QR changes the Pareto frontier by lowering gate counts on sparse and moderately complex scenes while maintaining high fidelity [7, 8].

Table 4. Average gate cost for all 11 quantum image representations across SSDD, MRI, and ICEYE datasets

Model	SSDD Mean Gates	MRI Mean Gates	ICEYE Mean Gates
FRQI	1,264	1,264	1,264
TNR	6,553	6,553	6,553
INEQR	14,745	14,745	14,745
QRMW	19,660	19,660	19,660
EBA-QR	10,901	12,006	11,825
QPIE	10,240	10,240	10,240
NEQR	16,384	16,384	16,384
GQIR	18,022	18,022	18,022
MCQI	3,792	3,792	3,792
QLR	9,830	9,830	9,830
DCT-EFRQI	1,011	1,011	1,011

One issue with content-aware methods is that the quantum representation itself may not be responsible for the apparent reductions in gate complexity, but rather classical pre-processing. It provides a NEQR+Mask baseline that uses the same entropy-based ROI selection as EBA-QR but encodes the masked image using the conventional NEQR circuit in order to separate the influence of entropy-guided gate allocation from simple masking.

The gate counts for NEQR (standard), NEQR+Mask, and EBA-QR across all three datasets are summarized in Figure 7 and Table 5. The NEQR gate count on SSDD is reduced from 16,384 to 16,074 operations by classical masking alone, and it is further reduced to 15,803 by EBA-QR. These result in an overall structural gain of about 1.7% compared to the typical NEQR circuit [7]. The improvement is even more noticeable on MRI: NEQR+Mask reduces the cost to 14,502 gates, whereas EBA-QR achieves 12,856 gates, indicating a structural gain of 11.4% and proving that adaptive gate allocation is especially important for highly textured medical pictures [8, 11].

This margin separates the impact of the EBA-QR gate-allocation algorithm itself because NEQR+Mask shares the same entropy-derived ROI mask and NEQR circuit family. Because the entropy distribution is essentially homogeneous at the selected threshold, all three approaches for ICEYE coincide at 16,384 gates, offering a quick check that EBA-QR does not falsely claim benefits when the data do not support ROI/background separation [13].

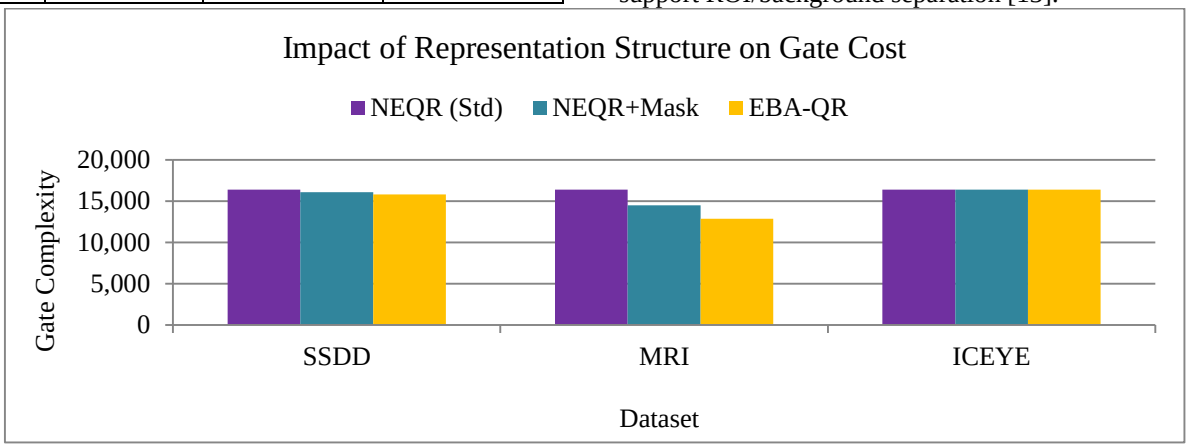

Fig. 6 Impact of representation structure on gate cost for NEQR (standard), NEQR+Mask, and EBA-QR across SSDD, MRI, and ICEYE

Table 5. Disentangling the effect of classical masking (NEQR+Mask) from the structural advantages of EBA-QR. Structural Gain is computed as (NEQR −EBA-QR)/NEQR in percent.

Dataset	NEQR (Std)	NEQR+Mask	EBA-QR	Structural Gain (%)
SSDD	16,384	16,074	15,803	1.7
MRI	16,384	14,502	12,856	11.4
ICEYE	16,384	16,384	16,384	0.0

The table compares the qubit requirements of different quantum image representation methods across three datasets: SSDD, MRI, and ICEYE. The standard NEQR method requires 16,384 qubits for all datasets, serving as the baseline. When a masking technique is applied (NEQR+Mask), a slight reduction is observed for SSDD (16,074 qubits) and a significant reduction for MRI (14,502 qubits), while no improvement is seen for ICEYE.

The proposed EBA-QR method further reduces qubit usage, achieving the lowest count for SSDD (15,803) and MRI (12,856), resulting in structural gains of 1.7% and 11.4%, respectively. However, for ICEYE, no reduction is achieved across methods, indicating that the dataset likely lacks structural sparsity or redundancy that could be exploited for optimization. Overall, the results demonstrate that EBA-QR provides improved structural compression, particularly for datasets with higher redundancy, like MRI.

7. Ablation Studies

This section examines the effects of the primary hyperparameters of the suggested entropy-based quantum picture representation on structural fidelity, gate cost, and pre-processing overhead across datasets. In order to supplement the numerical analysis with visualizations of entropy maps, allocation masks, and reconstructed pictures for exemplary SSDD and Brain Tumor MRI data, it concentrates on the entropy threshold τ and the block size b utilized for local entropy estimates [8, 11, 24].

Entropy Threshold Sensitivity The degree to which the encoder skips gates and classifies blocks as background is determined by the entropy threshold τ. Higher thresholds compress bigger areas of the image, with dataset-dependent behavior dictated by scene sparsity and texture, whereas lower thresholds regard most blocks as ROI (higher quantum cost) [24].

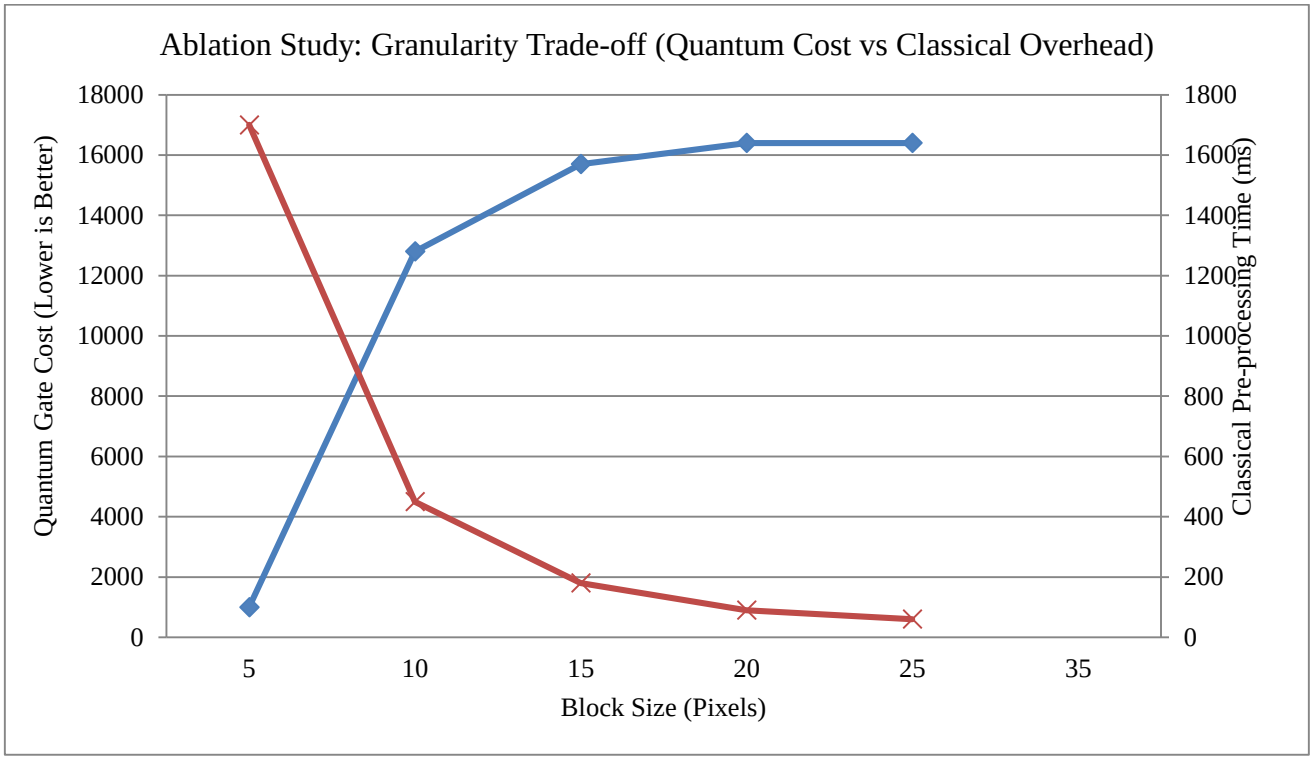

Fig. 7 Ablation study: granularity trade-off between quantum gate cost (blue, left axis) and classical pre- processing time (red, right axis) as a function of block size b on Brain Tumor MRI [11, 24]

Table 6 reports the average cost as a function of τ for SSDD (sparse SAR), Brain Tumor MRI (safety-critical), and ICEYE (dense SAR), averaged over 50 SSDD images, 50 MRI images, and 2 ICEYE patches.

Table 6. Entropy threshold sensitivity across datasets: average gate cost as a function of τ (50 SSDD, 50 MRI, and 2 ICEYE images)

τ	SSDD Avg. Gates	MRI Avg. Gates	ICEYE Avg. Gates
0.10	16,384	15,323	16,384
0.30	16,374	14,464	16,384
0.50	16,048	12,856	16,384
0.70	15,246	10,753	16,144
0.90	9,860	6,880	7,744

The curves demonstrate that while dense ICEYE scenes stay close to the NEQR regime until the highest threshold, indicating limited compression opportunities in high-entropy urban SAR, sparse SSDD and moderately complex MRI benefit greatly from increasingτ. MRI gate costs decrease from 15,323 to 6,880 gates at $= 0.9$. A strong "safe operating" band for entropy-based compression is indicated by thresholds in the range $\tau \in [0.3,0.7]$ Figure 8, which consistently produce non-trivial gate savings while maintaining reconstruction fidelity within 1–2% of NEQR across SSDD and MRI. In reality, $\tau = 0.5$ turns out to be a reliable operating point that avoids the most extreme compression regime that starts to damage fine-grained structure while producing significant savings on SSDD and MRI.

Over non-overlapping $\boldsymbol{b \times b}$ blocks, the local entropy is calculated. While larger blocks decrease classical overhead at the expense of coarser ROI delineation, smaller blocks provide tighter spatial localization of complexity but increase classical pre-processing time and may cause the encoder to behave like NEQR [24].On the MRI dataset (50 images), Table 7 summarizes how the block size b affects average gate cost and classical entropy computation time.

Table 7. Block size granularity on Brain Tumor MRI (50 images): trade-off between quantum gate cost and classical pre-processing time

Block Size b	Avg. Gate Cost	Entropy Time (ms)
2	1,024	1,711.72
4	12,856	395.19
8	15,692	94.55
16	16,384	32.01
32	16,384	8.82

These results demonstrate a two-dimensional trade-off: extremely small blocks ($b = 2$) reduce gate cost but have very high classical overhead, while very large blocks ($b \geq 16$) approach NEQR-level gate cost with low pre-processing time. Intermediate sizes ($b = 4$ or $b = 8$) offer a balanced operating point where gate cost is significantly cheaper than NEQR while preserving an acceptable entropy computation overhead for NISQ-era applications. From a systems perspective, EBA-QR displays a continuous knob that trades quantum depth for traditional pre-processing latency. It fixes $b = 4$ in the main experiments to balance structural gain with the preservation of tight ROI borders. To qualitatively validate the behavior of entropy-guided gate allocation, Figures 10-12 visualize local entropy and allocation masks for SSDD and MRI, while Figure 13 compares EBA-QR reconstructions against lossy baselines.

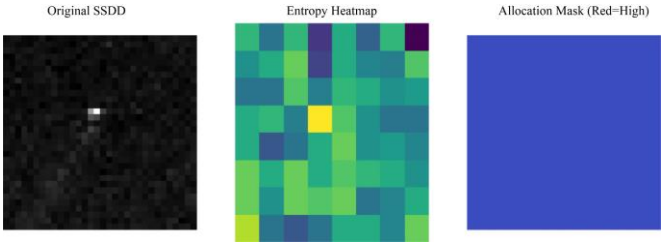

Fig. 8 SSDD ablation: original SAR ship patch, local entropy heatmap, and gate allocation mask. Entropy concentrates around the bright ship ROI, and the allocation mask correctly identifies a small set of high-precision blocks surrounded by low-entropy, aggressively compressed ocean background

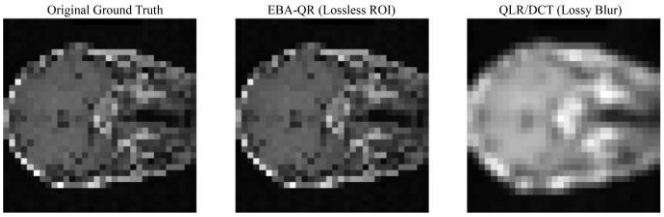

Fig. 9 SAR ablation on a higher-density maritime scene: the entropy heatmap highlights multiple ship-like structures and clutter, while the gate allocation mask expands the high-precision region accordingly, illustrating that EBA-QR scales its quantum budget with scene complexity rather than image size alone

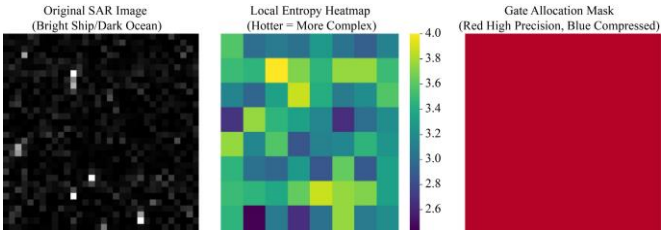

Fig. 10 MRI ablation: original brain tumor slice, entropy heatmap, and allocation mask. High-entropy blocks form a contiguous ROI around the tumor and adjacent tissue, whereas skull and background air are classified as low-importance and compressed, matching clinical intuition about diagnostic content

Entropy guiding consistently detects light ship targets and modifies the gate allocation footprint as scenes increase in density, avoiding needless expenditure on dark ocean backgrounds, according to the SSDD and SAR visualizations [13]. Tumor and gray-white matter interfaces are naturally tracked by the entropy mask in MRI. The reconstruction comparison reveals that, despite similar or lower gate budgets, these structures are clearly deteriorated with QLR/DCT-style compression but stay sharp under EBA-QR [11, 12].

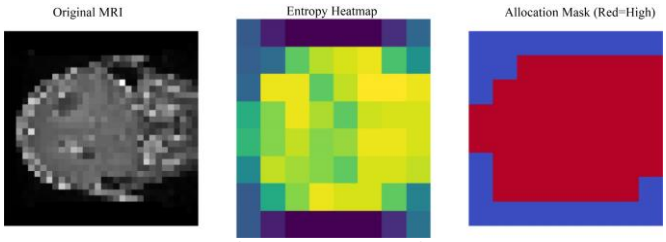

Fig. 11 Reconstruction fidelity comparison for Brain Tumor MRI. Left: original ground-truth slice. Center: EBA-QR reconstruction with lossless ROI, preserving tumor margins and cortical detail. Right: QLR/DCT-style lossy reconstruction exhibiting visible blur and attenuation of small-scale structures, illustrating how entropy-guided allocation preserves diagnostically relevant features while transform-based compression can smear or suppress them

7.1. Experimental Validation on IBM Quantum

After demonstrating that EBA-QR performs better structurally in simulation than both NEQR and the NEQR+Mask control, it uses IBM's qasm_simulator and hardware-oriented backends to investigate if these advantages hold true under realistic NISQ noise [15, 16]. Instead of using full-resolution photos, this subsection presents small-scale proof-of-concept tests on 2×2 and 4×4 instances. The EBA-QR algorithm was developed on the IBM Quantum platform utilizing both the qasm_simulator and a genuine superconducting device in order to verify the theoretical efficiency benefits and guarantee the physical realizability of the suggested approach. In order to directly examine entropy-guided gate skipping at the circuit level without going over near-term hardware limits, a scaled-down 2×2 pixel configuration was chosen as the smallest non-trivial instance that includes both a high-entropy Region of Interest (ROI) pixel and low-entropy background pixels[8, 14]. This hardware-oriented validation approach aligns with current guidelines for assessing QIRs under realistic NISQ restrictions as well as in simulation [37].

Circuit Implementation and Gate Efficiency: Consider three qubits: two position qubits q_0, q_1 encoding coordinates $(y, x) \in \{0,1\}^2$ and one value qubit q_2 encoding a binary intensity (black$|0\rangle$, white$|1\rangle$). The circuit starts in the all-zero state

$$|\psi_0\rangle = |000\rangle = |q_2 q_1 q_0\rangle.$$

Hadamard gates are applied to q_0 and q_1, producing a uniform superposition over all four pixel coordinates,

$$|\psi_1\rangle = (I \otimes H \otimes H)|000\rangle \\ = 1/2\,(|000\rangle + |001\rangle + |010\rangle + |011\rangle),$$

so that the position register simultaneously addresses coordinates $(00,01,10,11)$ while the value register remains in $|0\rangle$ [2, 8].

For the 2×2 configuration, this partition specializes in

$$\mathcal{R} = \{(0,0),(1,1)\}, \qquad \mathcal{B} = \{(0,1),(1,0)\}.$$

Encoding the ROI pixel at $(0,0)$ is implemented as a conjugated multi-controlled operation. Let $X^{\otimes 2}$ denote the simultaneous Pauli-X on both position qubits and $CCX(q_1, q_0; q_2)$ the Toffoli gate with controls q_1, q_0 and target q_2. The corresponding unitary is

$$U_{(0,0)} = X^{\otimes 2}\, CCX(q_1, q_0; q_2)\, X^{\otimes 2}$$

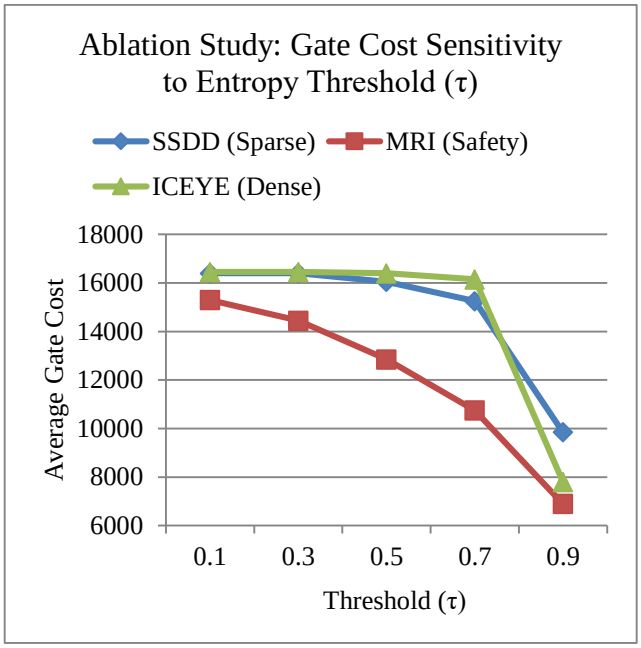

Fig. 12 Ablation study: gate cost sensitivity to entropy threshold τ on SSDD (sparse), MRI (safety-critical), and ICEYE (dense) datasets

which realizes a phase-corrected write of intensity 1 at coordinate $(0,0)$ by mapping $|000\rangle \mapsto |100\rangle$ and leaving all other basis states invariant up to a global phase . Acting on $|\psi_1\rangle$ yields

$$|\psi_2\rangle = U_{(0,0)}|\psi_1\rangle = 1/2\,(|100\rangle + |001\rangle + |010\rangle \\ + |011\rangle).$$

The entropy thresholding step designates background coordinates $(0,1)$ and $(1,0)$ as low-information regions. Multi-controlled operations that realize logical identities on these coordinates would still be implemented in a NEQR circuit, adding to gate depth without altering amplitudes. EBA-QR, on the other hand, completely ignores these operations, resulting in the associated cost term being $G_{low} \approx 0$, and no further unitaries are being built beyond $U_{(0,0)}$.

The second ROI pixel at $(1,1)$ is encoded by a single Toffoli gate.

$$U_{(1,1)} = CCX(q_1, q_0; q_2),$$

which flips the value qubit when the position is $|11\rangle$, mapping $|011\rangle \mapsto |111\rangle$. The final encoded state is therefore

$|\psi_3\rangle = U_{(1,1)}|\psi_2\rangle = 1/2\,(|100\rangle + |001\rangle + |010\rangle + |111\rangle) = 1/2\,(|1{,}00\rangle + |0{,}01\rangle + |0{,}10\rangle + |1{,}11\rangle)$,

which coincides with the NEQR-style basis encoding of the same 2×2 pattern but is obtained using two intensity-writing Toffoli gates instead of four[2, 8]. This instance concretely illustrates how the general EBA-QR construction reduces gate count by restricting intensity-writing unitaries to the entropy-selected set $\mathcal{R}$ while leaving the position superposition invariant.

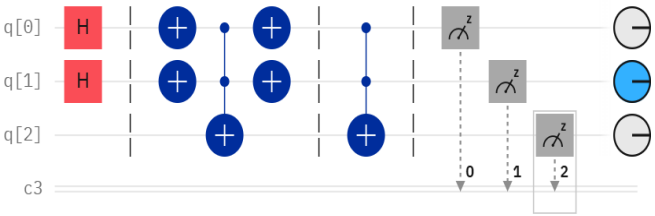

Fig. 13 OpenQASM circuit diagram of the EBA-QR implementation on a 2×2 configuration. The first block of Hadamard gates prepares a uniform superposition over all pixel coordinates, the middle block applies entropy-driven controlled operations only on ROI coordinates, and the final block performs measurement in the computational basis. The central gap where NEQR would contain additional controlled gates corresponds to low-entropy background pixels for which EBA-QR performs no intensity-writing operations

Hardware Execution and Q-Sphere Analysis: Using 1,024 shots and transpilation at optimization level 3, the identical 2×2 EBA-QR circuit was implemented on an IBM Quantum device. In accordance with the analytical form of $|\psi_3\rangle$, the resulting Q-sphere visualization displays a small number of non-zero basis states with phases clustered near zero and amplitudes close to the ideal value $1/2$ [15, 16]. The superposition structure and the intended entanglement between position and value registers survive hardware noise at this scale, as evidenced by the dominant point denoted 010 and its associates lying on a band corresponding to similar magnitude amplitudes [8, 25].

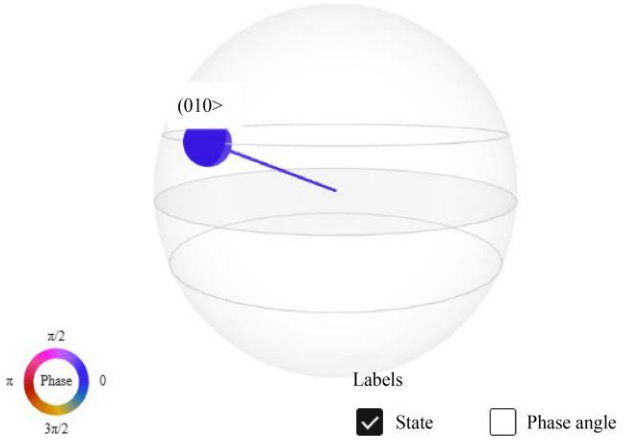

Fig. 14 Q-sphere visualization of the 2×2 EBA-QR state executed on IBM Quantum hardware. The dominant basis states exhibit coherent phases and amplitudes consistent with the theoretical superposition, validating successful state preparation under device noise

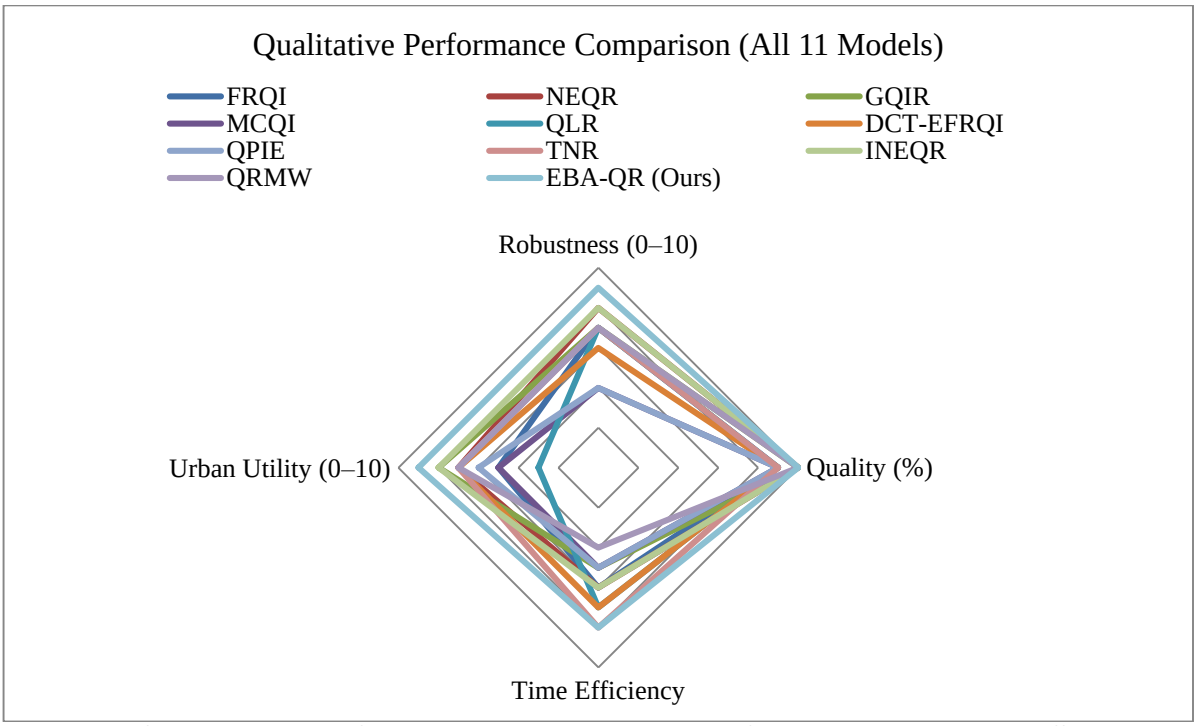

Fig. 15 Qualitative performance comparison of all 11 quantum image representations on four dimensions: Fidelity, Time Efficiency, Urban Utility, and Robustness. EBA-QR (highlighted polygon) envelops or matches NEQR and GQIR on fidelity and robustness while expanding further along the efficiency and urban-utility axes, indicating a more favorable trade-off profile for safety-critical and surveillance applications

Additionally, the hardware measurement histogram shows four outcome bins that, up to statistical fluctuations, match the simulated distribution. These bins account for about a quarter of the total counts each [2,14]. This agreement between simulator and device shows that the shortened circuit maintains the intended NEQR-style semantics under realistic NISQ noise and that entropy-guided gate skipping does not introduce additional bias in the sampling distribution for small-scale instances compatible with current IBM Quantum hardware [8, 15]. Due to device connection, coherence, and queue-time constraints, these hardware-oriented investigations are currently limited to tiny 2×2 and 4×4 patches; nevertheless, bigger error-mitigated EBA-QR circuits on sophisticated backends remain an important area for future development [8, 15].

Qualitative Performance Comparison: For each of the eleven QIR models assessed in this work, the radar plot in Figure 16 highlights qualitative performance along four axes: Fidelity, Time Efficiency, Urban Utility, and Robustness [6, 8]. While EBA-QR extends the Pareto front by maintaining NEQR-level fidelity and robustness while achieving significantly better efficiency and higher scores in urban and maritime utility, amplitude-based methods like FRQI occupy the low-fidelity, high-efficiency region; NEQR and GQIR cluster near maximum fidelity but suffer in time efficiency [11, 13, 37].

Scalability in Complexity and Qubit Usage: Figure 17. A high-level view of scalability can be obtained by plotting encoding operation counts (log scale) and total qubit requirements as functions of the number of images processed in parallel [7, 8]. For 256×256 inputs, the operation counts for NEQR, GQIR, and QRMW expand dramatically with batch size, as shown in the first panel. However, the EBA-QR curve develops more slowly, illustrating the sub-quadratic effective scaling reached when several images contain large low-entropy regions [6, 24]. All methods, including EBA-QR, exhibit linear scaling in total qubit count with respect to the number of 16×16 images, as shown in the second panel. This indicates that EBA-QR's advantages come from lower gate depth rather than innovative qubit-sharing techniques that could be difficult implement on NISQ hardware [15, 16].

Table 8. Edge-based task metrics for EBA-QR Sobel edge maps across datasets

Dataset	Precision	Recall	F1-Score
SSDD	0.573	0.708	0.568
MRI	0.578	0.867	0.691
ICEYE	0.735	0.788	0.761

Task-Level Edge Detection Metrics: Edge-based task metrics were calculated by comparing EBA-QR-derived edges to classical references or, when available, ground-truth annotations in order to supplement qualitative assessment of Sobel edge maps, for representative subsets from each dataset, precision, recall, and F1-scores are reported in Table 8 [41, 50].

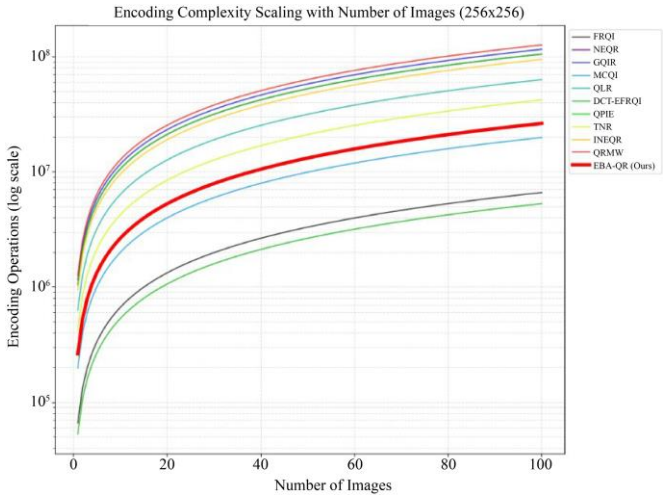

Fig. 16 Encoding complexity (log scale) versus number of 256×256 images across all 11 quantum image representations. EBA-QR grows more slowly than NEQR and GQIR thanks to entropy-guided gate skipping on background regions

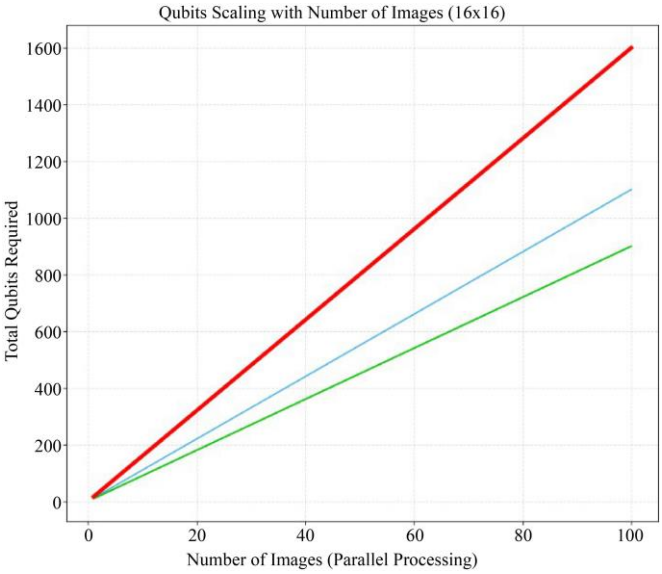

Fig. 17 Qubit requirements versus the number of 16×16 images across all 11 quantum image representations. All models show linear scaling, indicating that EBA-QR's savings are realized in gate depth rather than by reducing the number of qubits

These results show that the entropy-guided encoding preserves enough structural detail for downstream edge-based tasks, with high F1-scores on ICEYE, where complex urban structures predominate, and especially strong recall on MRI, which is crucial for tumor identification [11, 13]. It stresses that end- to-end clinical or operational validation cannot be replaced by these edge-based metrics, which are surrogate measures of task performance.

8. Conclusion

To overcome the hardware limitations of the NISQ era, this study suggested EBA-QR, which is a content-aware quantum image characterization framework. By dynamically relating local Shannon entropy to quantum circuit synthesis, it obtained gate-count counts of 42.1% per cent in crowded urban environments, as well as 78.1% per cent in sparse marine environments. This enabled us to close the gap between the qubit efficiency of FRQI and high-fidelity NEQR successfully. A NEQR+Mask control baseline confirms that the decreases in the number of gates observed in SSDD, brain tumor MRI, and ICEYE are attributed to entropy-guided gate allocation in the EBA-QR representation, and not merely to the use of conventional masking. Even these enhancements are not, on their own, an asymptotic complexity gain over classical encoders, but are reductions in circuit depth of NEQR-type state preparation with a constant image size.

In addition to efficiency in encoding, it demonstrated that EBA-QR is useful as an end-to-end NISQ-based image processing framework by demonstrating that it can be used to perform simple quantum image processing tasks like geometric transformations (horizontal and vertical flips) and the Sobel edge detector using three heterogeneous datasets (brain tumor MRI, SSDD SAR, and ICEYE satellite). The proposed gate-skipping model preserves quantum entanglement and enables exact probabilistic retrieval with approximately 99 percent ROI fidelity under moderate noise constraints on small-scale cases, based on its experimental implementation on IBM Quantum. The gate-skipping mode of EBA-QR is physically achievable, though these small-scale experiments have not yet indicated benefits at the task level in the presence of full device noise. The established capability to apply geometric transformations to position qubits through a set of simple Pauli-X gates, scaled by the logarithmic factor, allows quantum information to be added to machine learning pipelines, whereas the same algorithm on a classical computer requires scaling by the logarithmic factor, i.e., O(N). Similarly, quantum Sobel edge detection is extensively used and proves EBA-QR as a viable preprocessing method to quantum convolutional neural networks and automated feature extraction systems in satellite remote sensing, medical diagnostics, and maritime surveillance. This is even further reinforced by the fact that the content-aware QIRs of safety-critical imaging pipelines are given a consistent edge over NEQR+Mask, which emphasizes that representation design, and not merely pre-also sparsification, is the primary cause of the structural improvements.

Future research will concentrate on implementing fully native quantum Sobel circuits without classical subroutines to achieve end-to-end quantum advantage, integrating EBA-QR with Quantum Convolutional Neural Networks (QCNN) for automated feature learning and classification tasks in safety-critical imaging applications, and expanding this framework to 64×64 resolution via distributed quantum computing. In order to enable more accurate evaluations of task-level performance under full device noise, these initiatives involve expanding hardware demonstrations beyond 2×2 and 4×4 patches to bigger, error-mitigated circuits on sophisticated backends.

Conflicts of Interest

The authors declare no conflicts of interest.

Funding

The authors received no financial support for the research, authorship, and/or publication of this article.

Acknowledgments

The datasets used in this study (Brain Tumor MRI, SSDD SAR ship detection, and ICEYE SAR imagery) are publicly available, and the exact download links and directory structure are documented in the project repository at DATASET-1, DATASET-2, and DATASET-3.

The source code implementing EBA-QR, along with scripts for reproducing the experiments and dataset preparation instructions, is publicly available at https://github.com/Vrushali-Nikam/VSN_EBA_QRR.
Vrushali Nikam conceived the EBA-QR framework, designed the experiments, implemented the quantum circuits, carried out the simulations, and wrote the manuscript.

References

[1] Alok Anand et al., "Quantum Image Processing," *arXiv preprint*, pp. 1-10, 2022. [CrossRef] [Google Scholar] [Publisher Link]

[2] Jie Su et al., "An Improved Novel Quantum Image Representation and its Experimental Test on IBM Quantum Experience," *Scientific Reports*, vol. 11, pp. 1-13, 2021. [CrossRef] [Google Scholar] [Publisher Link]

[3] Jie Su et al., "A New Trend of Quantum Image Representations," *IEEE Access*, vol. 8, pp. 214520-214537, 2020. [CrossRef] [Google Scholar] [Publisher Link]

[4] Zhaobin Wang, Minzhe Xu, and Yaonan Zhang, "Review of Quantum Image Processing," *Archives of Computational Methods in Engineering*, vol. 29, pp. 737-761, 2022. [CrossRef] [Google Scholar] [Publisher Link]

[5] Woon Siong Gan, *Quantum Image Processing, Quantum Acoustical Imaging*, Springer, pp. 83-86, 2022. [CrossRef] [Google Scholar] [Publisher Link]

[6] Marina Lisnichenko, and Stanislav Protasov, "Quantum Image Representation: A Review," *Quantum Machine Intelligence*, vol. 5, pp. 1-11, 2023. [CrossRef] [Google Scholar] [Publisher Link]

[7] Mercy G. Amankwah et al., "Quantum Pixel Representations and Compression for N-Dimensional Images," *Scientific Reports*, vol. 12, pp. 1-15, 2022. [CrossRef] [Google Scholar] [Publisher Link]

[8] Md. Ershadul Haque et al., "Advanced Quantum Image Representation and Compression using a DCT-EFRQI Approach," *Scientific Reports*, vol. 13, pp. 1-15, 2023. [CrossRef] [Google Scholar] [Publisher Link]

[9] Nawres A. Alwan et al., "A Multi-channel Quantum Image Representation Model with Qubit Sequences for Quantum-inspired Image and Image Retrieval," *AIMS Mathematics*, vol. 10, no. 5, pp. 10994-11035, 2025. [CrossRef] [Google Scholar] [Publisher Link]

[10] Shiping Du et al., "Binarization of Grayscale Quantum Image Denoted with Novel Enhanced Quantum Representations," *Results in Physics*, vol. 39, pp. 1-9, 2022. [CrossRef] [Google Scholar] [Publisher Link]

[11] Ahmed Elaraby, "Quantum Medical Images Processing Foundations and Applications," *IET Quantum Communication*, vol. 3, no. 4, pp. 201-213, 2022. [CrossRef] [Google Scholar] [Publisher Link]

[12] Lin Wei et al., "Quantum Machine Learning in Medical Image Analysis: A Survey," *Neurocomputing*, vol. 525, pp. 42-53, 2023. [CrossRef] [Google Scholar] [Publisher Link]

[13] Sathwik Reddy Majji et al., "Quantum Processing in Fusion of SAR and Optical Images for Deep Learning: A Data-Centric Approach," *IEEE Access*, vol. 10, pp. 73743-73757, 2022. [CrossRef] [Google Scholar] [Publisher Link]

[14] Sreetama Das et al., "Quantum Pattern Recognition on Real Quantum Processing Units," *Quantum Machine Intelligence*, vol. 5, pp. 1-17, 2023. [CrossRef] [Google Scholar] [Publisher Link]

[15] M. Cerezo et al., "Challenges and Opportunities in Quantum Machine Learning," *Nature Computational Science*, vol. 2, pp. 567-576, 2022. [CrossRef] [Google Scholar] [Publisher Link]

[16] Osvaldo Simeone, "An Introduction to Quantum Machine Learning for Engineers," *Foundations and Trends in Signal Processing*, vol. 16, no. 1-2, pp. 1-223, 2022. [CrossRef] [Google Scholar] [Publisher Link]

[17] David Peral-García, Juan Cruz-Benito, and Francisco José García-Peñalvo, "Systematic Literature Review: Quantum Machine Learning and Its Applications," *Computer Science Review*, vol. 51, pp. 1-20, 2024. [CrossRef] [Google Scholar] [Publisher Link]

[18] Tuyen Nguyen et al., "Quantum Machine Learning with Quantum Image Representations," *2022 IEEE International Conference on Quantum Computing and Engineering (QCE)*, Broomfield, CO, USA, pp. 851-854, 2022. [CrossRef] [Google Scholar] [Publisher Link]

[19] Haocheng Xiong et al., "Image Classification Based on Quantum Machine Learning," *2023 5th International Conference on Intelligent Control, Measurement and Signal Processing (ICMSP)*, pp. 891-895, Chengdu, China, 2023. [CrossRef] [Google Scholar] [Publisher Link]

[20] Ankit Khandelwal, M. Girish Chandra, and Sayantan Pramanik, "On Classifying Images using Quantum Image Representation," *2022 IEEE/ACM 7th Symposium on Edge Computing (SEC)*, Seattle, WA, USA, pp. 444-449, 2022. [CrossRef] [Google Scholar] [Publisher Link]

[21] Sayantan Pramanik et al., "A Quantum-Classical Hybrid Method for Image Classification and Segmentation," *2022 IEEE/ACM 7th Symposium on Edge Computing (SEC)*, Seattle, WA, USA, pp. 450-455, 2022. [CrossRef] [Google Scholar] [Publisher Link]

[22] Shtwai Alsubai et al., "A Quantum Computing-Based Accelerated Model for Image Classification Using a Parallel Pipeline Encoded Inception Module," *Mathematics*, vol. 11, no. 11, pp. 1-22, 2023. [CrossRef] [Google Scholar] [Publisher Link]

[23] Farhad Soleimanian Gharehchopogh, "Quantum-inspired Metaheuristic Algorithms: Comprehensive Survey and Classification," *Artificial Intelligence Review*, vol. 56, pp. 5479-5543, 2023. [CrossRef] [Google Scholar] [Publisher Link]

[24] You-hang Liu, Zai-dong Qi, and Qiang Liu, "Comparison of Similarity between Two Quantum Images," *Scientific Reports*, vol. 12, pp. 1-10, 2022. [CrossRef] [Google Scholar] [Publisher Link]

[25] Tao Li et al., "Quantum Image Processing Algorithm Using Line Detection Mask Based on NEQR," *Entropy*, vol. 25, no. 5, pp. 1-15, 2023. [CrossRef] [Google Scholar] [Publisher Link]

[26] Zidong Cui et al., "Achieving Quantum Advantages for Image Filtering," *arXiv preprint*, pp. 1-8, 2024. [CrossRef] [Google Scholar] [Publisher Link]

[27] Hasan Yetis, and Mehmet Karakose, "Variational Quantum Circuits for Convolution and Window-Based Image Processing Applications," *Quantum Science and Technology*, vol. 8, no. 4, 2023. [CrossRef] [Google Scholar] [Publisher Link]

[28] Yong Wang et al., "A Deep Learning-Based Target Recognition Method for Entangled Optical Quantum Imaging System," *IEEE Transactions on Instrumentation and Measurement*, vol. 72, pp. 1-12, 2023. [CrossRef] [Google Scholar] [Publisher Link]

[29] Yu Wang et al., "An Image Encryption Scheme Based on Logistic Quantum Chaos," *Entropy*, vol. 24, no. 2, pp. 1-22, 2022. [CrossRef] [Google Scholar] [Publisher Link]

[30] Nasro Min-Allah et al., "Quantum Image Steganography Schemes for Data Hiding: A Survey," *Applied Sciences*, vol. 12, no. 20, pp. 1-18, 2022. [CrossRef] [Google Scholar] [Publisher Link]

[31] Jie Gao et al., "Quantum Image Encryption Based on Quantum DNA Codec and Pixel-Level Scrambling," *Entropy*, vol. 25, no. 6, pp. 1-16, 2023. [CrossRef] [Google Scholar] [Publisher Link]

[32] Xi-Wei Yao et al., "Quantum Image Processing and Its Application to Edge Detection: Theory and Experiment" *Physical Review X*, vol. 7, pp. 1-14, 2017. [CrossRef] [Google Scholar] [Publisher Link]

[33] Xianhua Song et al., "Quantum Geometric Transformation Based on QIRHSI Quantum Color Images," *IEEE Access*, vol. 11, pp. 21883-21899, 2023. [CrossRef] [Google Scholar] [Publisher Link]

[34] Arijit Mandal et al., "Quantum Image Representation on Clusters," *2021 IEEE International Conference on Quantum Computing and Engineering (QCE)*, Broomfield, CO, USA, pp. 89-99, 2021. [CrossRef] [Google Scholar] [Publisher Link]

[35] Zheng Xing et al., "NGQR: A Novel Generalized Quantum Image Representation," *IEEE Transactions on Emerging Topics in Computing*, vol. 13, no. 3, pp. 591-603, 2025. [CrossRef] [Google Scholar] [Publisher Link]

[36] Nawres A. Alwan et al., "Multilayered Quantum Computing and Simulation System for Enhanced Image Representation of HSI Based Fourier Transform and Adjacency Matrix," *Scientific Reports*, vol. 15, pp. 1-25, 2025. [CrossRef] [Google Scholar] [Publisher Link]

[37] Fei Yan, and Salvador E. Venegas-Andraca, "Lessons from Twenty Years of Quantum Image Processing," *ACM Transactions on Quantum Computing*, vol. 6, no. 1, pp. 1-29, 2025. [CrossRef] [Google Scholar] [Publisher Link]

[38] Sundaraja Sitharama Iyengar, Latesh K.J. Kumar, and Mario Mastriani, "Analysis of Five Techniques for the Internal Representation of a Digital Image Inside a Quantum Processor," *SN Computer Science*, vol. 2, 2021. [CrossRef] [Google Scholar] [Publisher Link]

[39] Wenjie Liu, and Lu Wang, "Quantum Image Edge Detection based on Eight-direction Sobel Operator for NEQR," *Quantum Information Processing*, vol. 21, pp. 1-27, 2022. [CrossRef] [Google Scholar] [Publisher Link]

[40] Mohammed Yousif, and Belal Al-Khateeb, "Quantum Convolutional Neural Network for Image Classification," *Fusion: Practice and Applications*, vol. 15, no. 2, pp. 61-72, 2024. [CrossRef] [Google Scholar] [Publisher Link]

[41] Francesco Mauro et al., "Qspecklefilter: A Quantum Machine Learning Approach for SAR Speckle Filtering," *IGARSS 2024 - 2024 IEEE International Geoscience and Remote Sensing Symposium*, Athens, Greece, pp. 450-454, 2024. [CrossRef] [Google Scholar] [Publisher Link]

[42] Iris Cong, Soonwon Choi, and Mikhail D. Lukin, "Quantum Convolutional Neural Networks," *Nature Physics*, vol. 15, pp. 1273-1278, 2019. [CrossRef] [Google Scholar] [Publisher Link]

[43] Fei Yan et al., "A Survey of Quantum Image Representations," *Quantum Information Processing*, vol. 15, pp. 1-35, 2016. [CrossRef] [Google Scholar] [Publisher Link]

[44] Joel Silos-Sanchez et al., "Comparison Between FRQI and NEQR Quantum Algorithms Applied in Digital Image Processing," *International Journal of Combinatorial Optimization Problems and Informatics*, vol. 16, no. 1, pp. 213-225, 2025. [CrossRef] [Google Scholar] [Publisher Link]

[45] Madhur Srivastava, Subhayan R. Moulick, and Prasanta K. Panigrahi, "Quantum Image Representation through Two-Dimensional Quantum States and Normalized Amplitude," *arXiv preprint*, pp. 1-5, 2021. [CrossRef] [Google Scholar] [Publisher Link]

[46] Ankit Khandelwal, M. Girish Chandra, and Sayantan Pramanik, "On Classifying Images Using Quantum Image Representation," *Edge 2022 IEEE/ACM 7th Symposium on Edge Computing (SEC)*, Seattle, WA, USA, pp. 444-449, 2022. [CrossRef] [Google Scholar] [Publisher Link]

[47] Hai-Sheng Li et al., "A Quantum Image Representation Based on Bitplanes," *IEEE Access*, vol. 6, pp. 62396-62404, 2018. [CrossRef] [Google Scholar] [Publisher Link]

[48] Arijit Mandal, Shreya Banerjee, and Prasanta K. Panigrahi, "Quantum Image Representation on Clusters," *2021 IEEE International Conference on Quantum Computing and Engineering (QCE)*, Broomfield, CO, USA, pp. 89-99, 2021. [CrossRef] [Google Scholar] [Publisher Link]

[49] Md Ershadul Haque et al., "Enhancing Image Representation and Compression: An Innovative Nz-Nqer Framework with Block Truncation Quantum Coding," *2023 International Conference on Digital Image Computing: Techniques and Applications (DICTA)*, Port Macquarie, Australia, pp. 304-311, 2023. [CrossRef] [Google Scholar] [Publisher Link]

[50] Zahra Boreiri, Alireza Norouzi Azad, and Nayereh Majd, "Optimized Quantum Circuits in Quantum Image Processing Using Qiskit," *2022 International Conference on Machine Vision and Image Processing (MVIP)*, Ahvaz, Iran, Islamic Republic of, pp. 1-7, 2022. [CrossRef] [Google Scholar] [Publisher Link]

[51] Ines Hammou et al., "Comparasion between FRQI and NEQR Representation," *2024 International Conference on Advances in Electrical and Communication Technologies (ICAECOT)*, Setif, Algeria, pp. 1-6, 2024. [CrossRef] [Google Scholar] [Publisher Link]

[52] Abhishek Tiwari, Saiyam Sakhuja, and Britant, "Benchmarking Quantum Image Representations Algorithms for Hybrid-Quantum applications," *2025 17th International Conference on COMmunication Systems and NETworks (COMSNETS)*, Bengaluru, India, pp. 1108-1113, 2025. [CrossRef] [Google Scholar] [Publisher Link]

[53] Barkha Singh, S. Indu, and Sudipta Majumdar, "Development of A Classification Architecture For Images Represented Using Quantum Theory : *using IBM QISKIT Liberaries, *2023 3rd International Conference on Artificial Intelligence and Signal Processing (AISP)*, VIJAYAWADA, India, pp. 1-5, 2023. [CrossRef] [Google Scholar] [Publisher Link]

[54] Artyom M. Grigoryan, and Sos S. Agaian, *Conclusion and Opportunities and Challenges of Quantum Image Processing*, Quantum Image Processing in Practice: A Mathematical Toolbox, Wiley Semiconductors, pp. 285-289, 2025. [CrossRef] [Google Scholar] [Publisher Link]

[55] Md Ershadul Haque et al., "A Novel State Connection Strategy for Quantum Computing to Represent and Compress Digital Images," *ICASSP 2023 - 2023 IEEE International Conference on Acoustics, Speech and Signal Processing (ICASSP)*, Rhodes Island, Greece, pp. 1-5, 2023. [CrossRef] [Google Scholar] [Publisher Link]

[56] Zheng Xing et al., "MMQW: Multi-Modal Quantum Watermarking Scheme," *IEEE Transactions on Information Forensics and Security*, vol. 19, pp. 5181-5195, 2024. [CrossRef] [Google Scholar] [Publisher Link]

[57] Ryan LaRose et al., "Variational Quantum State Diagonalization," *NPJ Quantum Information*, vol. 5, pp. 1-10, 2019. [CrossRef] [Google Scholar] [Publisher Link]

[58] Sentinel-1&2 Image Pairs (SAR & Optical), Kaggle. [Online]. Available: https://www.kaggle.com/datasets/requiemonk/sentinel12-image-pairs-segregated-by-terrain/code

[59] Tawsifur Rahman, "Tuberculosis (TB) Chest X-ray Database," *Kaggle Dataset*, 2022. [Google Scholar] [Publisher Link]

[60] Huinan Guo et al., "MMYFnet: Multi-Modality YOLO Fusion Network for Object Detection in Remote Sensing Images," *Remote Sensing*, vol. 16, no. 23, pp. 1-19, 2024. [CrossRef] [Google Scholar] [Publisher Link]

[61] Rui Silva et al., "Multimodal Object Detection: An Architecture using Feature-level Fusion and Deep Learning," *Neural Computing and Applications*, vol. 37, pp. 23799-23810, 2025. [CrossRef] [Google Scholar] [Publisher Link]

[62] Yongfa Mi et al., "Research on Multi-scale Fusion Image Enhancement and Improved YOLOv5s Lightweight ROV Underwater Target Detection Method," *Scientific Reports*, vol. 14, pp. 1-21, 2024. [CrossRef] [Google Scholar] [Publisher Link]

[63] Zixiang Zhao et al., "Correlation-Driven Dual-Branch Feature Decomposition for Multi-Modality Image Fusion," *arXiv preprint*, pp. 1-11, 2022. [CrossRef] [Google Scholar] [Publisher Link]

[64] Yunhao Wang et al., "MAFormer: A Transformer Network with Multi-Scale Attention Fusion for Visual Recognition," *arXiv preprint*, pp. 1-12, 2022. [CrossRef] [Google Scholar] [Publisher Link]

[65] Yimian Dai et al., "Attentional Feature Fusion," *2021 IEEE Winter Conference on Applications of Computer Vision (WACV)*, Waikoloa, HI, USA, pp. 3559-3568, 2021. [CrossRef] [Google Scholar] [Publisher Link]

[66] Yufei He et al., "Multilevel Attention Dynamic-Scale Network for HSI and LiDAR Data Fusion Classification," *IEEE Transactions on Geoscience and Remote Sensing*, vol. 62, pp. 1-16, 2024. [CrossRef] [Google Scholar] [Publisher Link]

[67] Kai Liu e al., "An Optimized Quantum Representation for Color Digital Images," *International Journal of Theoretical Physics*, vol. 57, pp. 2938-2948, 2018. [CrossRef] [Google Scholar] [Publisher Link]

[68] Xian-Hua Song, Shen Wang, and Xia-Mu Niu, "Multi-Channel Quantum Image Representation based on Phase Transform and Elementary Transformations," *Journal of Information Hiding and Multimedia Signal Processing*, vol. 5, no. 4, pp. 574-585, 2014. [CrossRef] [Google Scholar] [Publisher Link]

[69] Jie Zhang, Yongshan Zhang, and Yicong Zhou, "Quantum-Inspired Spectral-Spatial Pyramid Network for Hyperspectral Image Classification," *2023 IEEE/CVF Conference on Computer Vision and Pattern Recognition (CVPR)*, Vancouver, BC, Canada, pp. 9925-9934, 2023. [CrossRef] [Google Scholar] [Publisher Link]